Geochemistry Geophysics Geosystems G3

Article
Volume 14, Number 5
6 May 2013
doi:10.1002/ggge.20105
ISSN: 1525-2027

Published by AGU and the Geochemical Society

Termination of a 6 year ridge-spreading event observed using a seafloor seismic network on the Endeavour Segment, Juan de Fuca Ridge

Robert T. Weekly
Department of Earth and Space Sciences, University of Washington, Box 351310, Seattle, Washington, 98195-1310, USA (rtweekly@uw.edu)

William S. D. Wilcock
School of Oceanography, University of Washington, Seattle, Washington, USA

Emilie E. E. Hooft and Douglas R. Toomey
Department of Geological Sciences, University of Oregon, Eugene, Oregon, USA

Paul R. McGill
Monterey Bay Aquarium Research Institute, Moss Landing, California, USA

Debra S. Stakes
Earth and Ocean Sciences Program, Division of Physical Sciences, Cuesta College, San Luis Obispo, California, USA

[1] We present automatically determined epicenters and magnitudes for 36,523 earthquakes recorded along the Endeavour segment between August 2003 and October 2006 using a local ocean-bottom seismometer (OBS) network. The catalog is dominated by two swarm sequences in January and February 2005 in the vicinity of the Endeavour overlapping spreading center, which included earthquakes in West Valley, the northern portion of the Endeavour segment, southwest Endeavour Valley, and the Endeavour vent fields. These swarms are attributed to volcanism including a dike intrusion on the northern Endeavour in February 2005 and smaller diking events on the propagating tip of the West Valley segment in both swarms. The dike on the northern Endeavour propagated to the south, which is inconsistent with magma sourced from the axial magma chamber beneath the elevated central portion of the segment. Following the swarms, seismic activity on the Endeavour segment decreased on average to ~15% of pre-swarm values and almost ceased at the segment ends. We infer that a 6 year non-eruptive event that started with a swarm in 1999 and finished with the 2005 swarms ruptured the entire segment and relieved plate-spreading stresses. The inferred coupling between the 1999 and 2005 events, the observation of extensive precursory activity prior to the 2005 swarms, and the interaction between seismically active regions during the swarms is consistent with static triggering with delays influenced by viscoelastic relaxation, hydraulic diffusion, and magma withdrawal and replenishment.

Components: 15,000 words, 10 figures, 3 tables.

Keywords: ridge; earthquake; spreading.

Index Terms: 3035 Marine Geology and Geophysics: Midocean ridge processes; 3075 Marine Geology and Geophysics: Submarine tectonics and volcanism; 7220 Seismology: Oceanic crust; 7245 Seismology: Mid-ocean ridges.

Received 24 May 2012; **Revised** 18 February 2013; **Accepted** 24 February 2013; **Published** 6 May 2013.

Weekly, R. T., W. S. D. Wilcock, E. E. E. Hooft, D. R. Toomey, P. R. McGill, and D. S. Stakes (2013), Termination of a 6 year ridge-spreading event observed using a seafloor seismic network on the Endeavour Segment, Juan de Fuca Ridge, *Geochem. Geophys. Geosyst.*, *14*, 1375–1398, doi:10.1002/ggge.20105.

1. Introduction

[2] Earthquakes occurring along mid-ocean ridges result from the release of stress within the brittle portion of oceanic lithosphere. Plate-spreading processes that contribute to stress accumulation include extensional tectonics [*Barclay et al*., 2001; *deMartin et al*., 2007; *Toomey et al*., 1988; *Wolfe et al*., 1995], magmatic activity [*Dziak and Fox*, 1999a; 1999b; *Dziak et al*., 2004; *Sohn et al*., 1998a; *Wilcock et al*., 2009], and hydrothermal circulation [*Sohn et al*., 1998b; *Tolstoy et al*., 2008; *Tolstoy et al*., 2006; *Wilcock et al*., 2002]. The relative contributions of each process to the local stress field is determined by spreading rate [*Tolstoy*, 2008b], and each of these processes produce distinct patterns of seismicity.

[3] Along slow-spreading-rate ridges (1–4 cm/yr full rate) [*Macdonald*, 2001], such as the Mid-Atlantic Ridge (MAR), the rate of spreading is believed to be insufficient to sustain a steady state axial magma chamber (AMC) [*Phipps Morgan and Chen*, 1993; *Sinton and Detrick*, 1992]. Stress accumulation and axial valley morphology are influenced by alternating episodes of volcanism and tectonic extension [*Karson et al*., 1987; *Smith and Cann*, 1992, 1993]. Earthquakes observed on the MAR have magnitudes up to about M_w = 5, extend up to 8 km deep beneath the axial valley and adjacent rift mountains, and have focal mechanisms consistent with normal faulting [*Barclay et al*., 2001; *deMartin et al*., 2007; *Huang et al*., 1986; *Toomey et al*., 1985; *Wolfe et al*., 1995]. Large magnitude events tend to be followed by aftershock sequences that show a modified Omori law decay pattern and yield *b*-values of ~1.0 [*Bohnenstiehl et al*., 2002].

[4] At fast- (>9 cm/yr full rate) and intermediate- (4–9 cm/yr full rate) spreading-rate ridges, extension is primarily accommodated via episodic diking events driven by a steady state crustal AMC [*Delaney et al*., 1998; *Sinton and Detrick*, 1992]. The earthquakes are smaller because the lithosphere is thin and a large proportion of fault slip occurs aseismically [*Cowie et al*., 1993; *Tolstoy*, 2008b]. Between episodic diking events, the highest concentration of microearthquakes occurs directly above the AMC in the shallow crust and is associated with thermomechanical strain induced by a combination of hydrothermal cooling [*Sohn et al*., 2004; *Wilcock et al*., 2002] and magma chamber inflation [*Wilcock et al*., 2009]. Because of the importance of diking events in crustal formation and interest in understanding their impacts on seafloor hydrothermal and biological processes [*Delaney et al*., 1998], considerable efforts have been made to respond to these events [*Cowen et al*., 2004] and understand their characteristics. Earthquakes associated with seafloor eruptions have been investigated using local seismic networks or regional hydroacoustic arrays on the East Pacific Rise (EPR) at 9°50′N [*Tolstoy et al*., 2006], the Juan de Fuca Ridge [*Dziak and Fox*, 1999b; *Dziak et al*., 1995; *Dziak et al*., 2011; *Sohn et al*., 1999], and the Gorda Ridge [*Fox and Dziak*, 1998]. Diking events are marked by the onset of intense earthquake swarms that lack a discernible mainshock-aftershock sequence, and the magnitude-frequency distribution of these swarms yield *b*-values significantly greater than unity [*Bohnenstiehl et al*., 2002]. The rate of seismicity can build for several years prior to an eruption with precursory swarms lasting a few hours, while the dike injection occurs over the course of 1–2 weeks and is accompanied by extensive seismicity with rates >25 events/hr [*Dziak and Fox*, 1999a]. Post-eruption seismicity rates decline sharply and return to background levels on timescales of several months as the crust returns to thermal equilibrium [*Sohn et al*., 1998a].

[5] In contrast to diking events that feed seafloor eruptions, the seismicity associated with intrusive diking events has not been extensively studied. A

notable exception is the Endeavour segment of the Juan de Fuca Ridge where swarms in June 1999 and January 2000 [*Bohnenstiehl et al.*, 2004; *Johnson et al.*, 2000] and February 2005 [*Hooft et al.*, 2010] were investigated with hydroacoustic recordings and a local seismic network, respectively. In this paper, we present a 3 year catalog of seismicity obtained with an automated algorithm devised to process a large amount of data recorded by a local seafloor OBS network deployed on the Endeavour segment from 2003 to 2006. The catalog includes two substantial swarms in January and February 2005. We discuss the characteristics of the two swarms and their contribution to the spreading cycle, compare them to magmatic events in other locations, and discuss the role of precursory activity and triggering.

2. The Endeavour Segment

2.1. Regional Geology

[6] The Juan de Fuca Ridge (JdFR) is an intermediate-rate (5.7 cm/yr) [*DeMets et al.*, 1994] spreading center located in the northeast Pacific Ocean that forms the boundary between the Pacific and Juan de Fuca plates (Figure 1a, inset). The JdFR is comprised of seven individual spreading segments that are bounded by large OSCs. The regional tectonics of the northern JdFR are complicated by the presence of an unstable triple junction [*Hyndman et al.*, 1979] where the Sovanco and Nootka transform faults intersect the ridge and by north-south compression resulting from the relative motions of the Pacific and Explorer plates [*Kreemer et al.*, 1998].

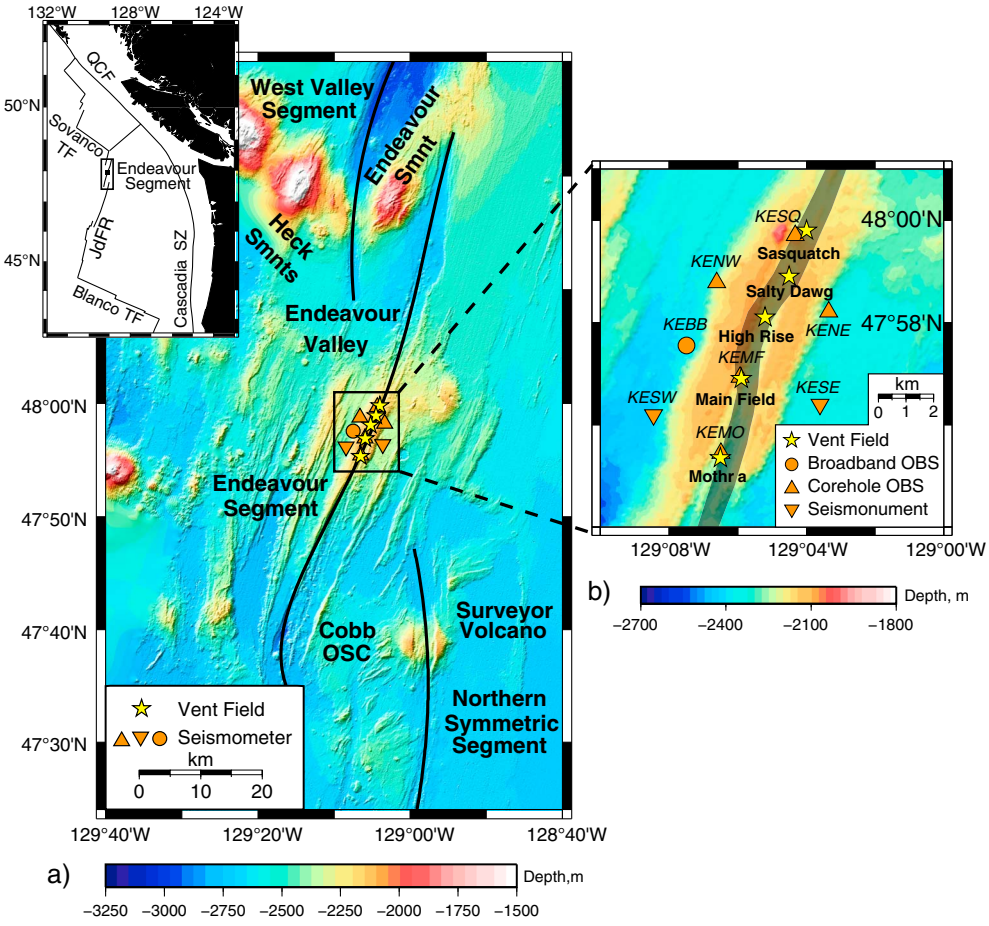

Figure 1. (a) Bathymetric map of the Endeavour segment showing the Keck seismometer network (orange symbols) and high-temperature vent fields (yellow stars) on the central portion of the segment. Black lines show plate boundaries and the black box shows the area in Figure 1b. The inset figure shows the regional setting of the Endeavour segment at the northern end of the Juan de Fuca Ridge. (b) Bathymetric map of vent field area showing the seismometer network with station names is labeled in italics, and high-temperature vent fields are labeled in bold. The extent of the axial magma chamber [*Van Ark et al.*, 2007] is indicated by gray shadow. Bathymetry is from the Seabeam data set collected by the NOAA/VENTS program.

[7] The Endeavour Segment is a 90 km long spreading segment located near the northern end of the JdFR (Figure 1a). The segment is bounded to the north and south by the Endeavour and Cobb OSCs, respectively, with several prominent seamount chains located on its western flank. The central portion of the segment comprises a series of ridge-parallel abyssal hills and valleys spaced ~6 km apart [*Karsten et al*., 1986]. This ridge-basin sequence overlies an elevated plateau with thickened crust that extends out to ages of 0.7 Ma [*Carbotte et al*., 2008]. It has been proposed that magma supply is enhanced because the ridge has overridden the mantle melt anomaly that generated the Heckle Seamount chain [*Carbotte et al*., 2008; *Karsten and Delaney*, 1989].

[8] At the center of the segment, five high-temperature (>300°C) black smoker fields are spaced 2–3 km apart within the 1 km wide, 75 m deep axial valley (Figure 1b) with several low-temperature (<100°C) diffusely venting sites interspersed between the fields [*Delaney et al*., 1992; *Glickson et al*., 2007; *Kelley et al*., 2001; *Kelley et al*., 2002; *Robigou et al*., 1993]. From north to south, the fields are named Sasquatch, Salty Dawg, High Rise, Main Endeavour Field, and Mothra (Figure 1b). *Wilcock and Delaney* [1996] suggested that tectonic faulting and downward propagation of a cracking front into a solidified magma chamber controlled heat supply and hydrothermal circulation beneath the vent fields. More recently, however, a multi-channel seismic dataset imaged an AMC underlying all of the vent fields at a depth of 2–3 km beneath the seafloor [*Carbotte et al*., 2006; *Van Ark et al*., 2007]. The presence of an AMC suggests that a substantial amount of magmatic heat is being supplied to the hydrothermal system and that volcanism is an integral component of present-day plate spreading and seismogenesis at the Endeavour segment.

2.2. Seismicity

[9] The U.S. Navy's Sound Surveillance System (SOSUS) hydrophone network provides a record of ~50,000 earthquakes larger than magnitude ~2 that have occurred along the Juan de Fuca Ridge since 1991 [*Dziak et al*., 2011]. With the exception of Axial Seamount, the southern and central segments of the JdFR have been seismically active only during periods of volcanism. In contrast, the northern portion of the JdFR, including the Endeavour, has been continually seismically active and the locus of many seismic swarms.

[10] Two periods of particular interest are swarm sequences recorded between June 1999 and January 2000 along the central and southern portions of the Endeavour segment [*Bohnenstiehl et al*., 2004; *Johnson et al*., 2000], and between January and March 2005 along the northern Endeavour and adjacent southern West Valley Segments [*Hooft et al*., 2010]. Although *Johnson et al*. [2000] originally interpreted the June 1999 swarm as having a tectonic source, the frequency-magnitude distribution of earthquakes [*Bohnenstiehl et al*., 2002], strain-induced pressure changes in regional boreholes [*Davis et al*., 2001], and perturbations to the fluid chemistry and volatile content [*Lilley et al*., 2003; *Seewald et al*., 2003; *Seyfried et al*., 2003] are consistent with a non-eruptive diking event. *Bohnenstiehl et al*. [2004] argue that dike propagation associated with the June 1999 swarm increased post-seismic Coulomb stress levels immediately to the south of the swarm terminus and led to a second swarm in January 2000 that had a more limited along-axis extent.

[11] In addition to the SOSUS records, the 2005 swarms were recorded by a local OBS network. *Hooft et al*. [2010] located over 6000 earthquakes for the February swarm using manual picks. The spatial and temporal pattern of earthquakes is complex with the locus of seismicity evolving over the course of the swarm as earthquakes occur near the Endeavour Seamount and West Valley Segment, on the northern Endeavour Segment, within the Endeavour Valley, and under the vent fields. The majority of moment release, including the six largest earthquakes that have strike-slip mechanisms, occurred at the southwest end of the Endeavour Valley near the southern extension of the West Valley Segment. However, the magnitude and polarity of borehole pressure anomalies and their timing relative to the onset of seismicity indicated a dike intrusion on the northern portion of the Endeavour Segment [*Hooft et al*., 2010]. The February 2005 swarm triggered earthquakes and a hydrologic response within the vent fields. An increase in vent field seismicity occurred within ~2.5 days of the onset of the swarm, coincident with a modest temperature increase (~4 °C) at a diffuse vent in the Mothra field. *Hooft et al*. [2010] interpret this delay between swarm onset and observed thermal anomalies as the time required for a hydrologic pressure perturbation to diffuse along the ridge.

[12] A number of studies at the Endeavour Segment have employed local OBS networks to study microearthquakes associated with hydrothermal venting [*McClain et al*., 1993; *Wilcock et al*., 2002; *Wilcock et al*., 2009]. *McClain et al*. [1993] argued that ongoing tectonic extension maintains the conduits

necessary for sustained fluid circulation and formation of mature hydrothermal vent fields. A 55 day study in 1995 located nearly 1000 earthquakes concentrated at ~2 km depth beneath the axial valley with focal mechanisms that were consistent with plate-spreading and tensile stresses due to hydrothermal cooling [*Wilcock et al.*, 2002]. Focal mechanisms for 170 events occurring beneath the hydrothermal vent fields during 2003–2004 similarly delineate a zone of ridge-perpendicular horizontal tension [*Wilcock et al.*, 2009]. However, this region was bracketed by zones of compression on the ridge flanks, which suggests that seismicity at the ridge axis results from magmatic inflation of the AMC rather than tectonic extension [*Wilcock et al.*, 2009].

3. Keck Seismic Network

[13] From August 2003 to October 2006, an eight-station, 10 km aperture array was deployed along the central portion of the Endeavour Segment of the Juan de Fuca Ridge (Figure 1b). The array comprised seven short-period three-component corehole ocean-bottom seismometers (OBS) deployed in horizontal drill holes or concrete "seismonuments" [*Stakes et al.*, 1998] and one buried broadband Guralp CMG-1T OBS [*Romanowicz et al.*, 2006; *Stakes et al.*, 2002]. The short-period sensor comprised three orthogonal Mark Products L-28LB geophones that have a flat frequency response from 1 to 90 Hz and were sampled at 128 Hz. The broadband sensor was a three-component Guralp CMG-1T that has a flat frequency response from 2.8 mHz–50 Hz and was sampled at either 50 or 100 Hz.

[14] The Keck network was deployed in a novel way using remotely operated vehicles (ROVs) instead of traditional free-fall seismometer deployment methods [*Wilcock et al.*, 2007]. This ensured strong coupling of the sensors to the seafloor and enabled measurement of horizontal sensor orientation. Using ROVs for annual deployments ensured that the network continued to record high-quality data comparable to land-based seismometer networks for over 39 consecutive months and allowed the determination of a microearthquake catalog that to date, spans a longer period of time than any other earthquake catalog derived from a seafloor OBS network. There were, however, periods of instrument failures in years 2 and 3 that are summarized in Table 1.

[15] To correct for timing errors, we calculated clock corrections by assuming a constant drift rate between each deployment and recovery. We were unable to obtain clock offsets upon recovery of station KEBB after the second year and stations KEMF, KENE, KENW, and KESE after the third year due to instrument power loss before recovery. For stations KENE, KENW, and KESE in year 3, clock drift rates were obtained using the known times of 190 shots (40 in^3 source volume) obtained in July 2006 with the *R/V Tully*. Clock drift rates for stations KEBB in year 2 and KEMF in year 3 were calculated iteratively during the earthquake analysis by fitting a trend to the mean daily misfit between observed and predicted times for earthquake arrivals.

4. Methods

[16] In order to process the data efficiently, we implement an automatic algorithm which locates earthquakes using *Hypoinverse* [*Klein*, 2002] with a layered velocity model derived from earlier

Table 1. Summary of Instrument Failures

	Year 1	Year 2	Year 3
Station	(August 2003–August 2004)	(August 2004–September 2005)	(September 2005–October 2006)
KEMO	-	Low S/N	-
KEMF	-	Low S/N	No data June 10–October 31
KESQ	-	No data	-
KESW	-	No data December 9–February 28	-
KESE	-	-	No data
KENW	-	-	-
KENE	-	-	-
KEBB	No data May 31–August 9	No data March 14–September 26	No data

Station locations are shown in Figure 1b. Periods during the deployment when instruments were not operating or recording degraded data are noted. Calendar dates are used to indicate periods when data are unavailable for a portion of a deployment. Low S/N indicates that the signal to noise was low because the gain was set very low so that only the largest events were recorded.

studies (Figure 2); the method is described in detail in the supplementary documents. The algorithm uses the ratio of the root-mean-squared (RMS) amplitudes in short-term and long-term windows to trigger on impulsive arrivals, associates triggers observed on multiple stations as events and distinguishes earthquakes from ~20 Hz whale calls [*Cummings and Thompson*, 1971; *Watkins et al.*, 1987] on the basis of frequency content. For each earthquake, it picks potential *P* and *S* wave arrival times based on sharp increases in the smoothed RMS amplitude and with an autoregressive method [*Takanami and Kitagawa*, 1988], assigns pick weights on the basis of signal-to-noise, and systematically searches for an earthquake location that maximizes the number of adequately modeled picks. Earthquakes located more than 3 km from the nearest station are assigned a fixed focal depth of 3 km, the average depth of earthquakes determined both on axis and off axis in an earlier study [*Wilcock et al.*, 2002]. The final catalog uses *P* and *S* wave picks obtained from the autoregressive and RMS amplitude methods, respectively, because these choices minimized the RMS-weighted phase residuals. *S* wave picks were downweighted by a factor of 0.5 to account for their greater uncertainty. The catalog includes only earthquakes located with a minimum of six picks of which at least two must be

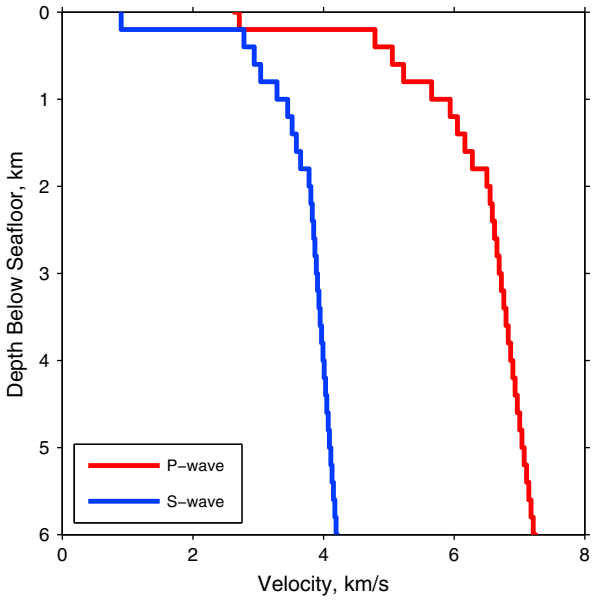

Figure 2. *P* (red line) and *S* wave (blue line) velocity models used for determining earthquake locations using *Hypoinverse* [*Klein*, 2002]. The *P* wave model is derived from a previous refraction experiment [*Cudrak and Clowes*, 1993], while the *S* wave model is derived assuming V_P/V_S = 3.0 above 0.4 km and V_P/V_S = 1.72 below 0.4 km [*Wilcock et al.*, 2009].

P waves and two must be *S* waves. Station corrections are included which were calculated iteratively to account for local structure beneath stations and systematic pick biases (see Table S1 in the supporting information).[1] The catalog completeness is comparable to manual catalogs obtained by student analysts [*Hooft et al.*, 2010; *Wilcock et al.*, 2009] (see supporting information).

[17] To estimate hypocentral uncertainties, *Hypoinverse* [*Klein*, 2002] requires a value for the "picking" error, σ, of a *P* wave arrival. This accounts for all sources of error including the errors in reading the onset of arrivals, clock errors, and errors arising from modeling travel times using a simplified one-dimensional velocity model and a flat datum. Following [*Sohn et al.*, 1998a], we calculate this value according to

$$\sigma^2 = \frac{\sum_{i=1}^{n}\sum_{j=1}^{m_i} w_{i,j}^2 \Delta t_{i,j}^2}{\sum_{i=1}^{n}(m_i - p)} \quad (1)$$

where w is the weight assigned to an arrival (the product of the pick weight, phase weight, and any downweighting applied by *Hypoinverse*), Δt is the travel time residual, m is the number of arrival time observations for a particular earthquake, n is the number of earthquakes, p is the number of free parameters being solved for, and i and j are indices of the earthquake and arrival time observation, respectively. We obtain a value of 95 ms for our full catalog, which likely reflects the strong velocity heterogeneity in the region [*Weekly et al.*, 2011].

[18] Seismic moments are calculated using attenuation-corrected *P* and *S* wave spectral amplitudes [*Brune*, 1970; *Hanks and Wyss*, 1972], following the methods and values developed for previous MOR earthquake studies [*Hooft et al.*, 2010; *Toomey et al.*, 1988; *Tréhu and Solomon*, 1983; *Wilcock et al.*, 2002]. The seismic moment (M_o) for each *P* or *S* wave arrival on a station is given by

$$M_O = \frac{4\pi\rho x c^3 \Omega_0}{KR} \quad (2)$$

where ρ is the rock density at the hypocentral source, x is the epicentral distance to the earthquake, c is seismic wave speed, Ω_0 is the spectral amplitude in the 4–10 Hz frequency band corrected for attenuation, K represents a free-surface correction, and R is a radiation pattern factor. The parameter values based on *Toomey et al.* [1985] are shown in Table 2. The seismic moment for an

[1] All supporting information may be found in the online version of this article.

Table 2. Parameters Used to Obtain Earthquake Magnitudes

Parameter	*P*	*S*
ρ (g/cm^3)	3	3
c (km/s)	6.5	3.7
R	0.42	0.59
K	1.5	1.7
Q	(30 500)	(50 400)
f (Hz)	4–10	4–10

Values appropriate for mid-ocean ridge setting were taken from *Toomey et al*. [1985]. ρ is the rock density, c is the seismic wave speed, R is a radiation factor, K is a free-surface correction, Q is a two-element attenuation model with the first value assumed within 1 km of the receiver and the second value elsewhere, and f is the frequency band used to obtain spectral amplitudes.

earthquake is equal to the average of the median values of M_o for *P* waves and for *S* waves.

[19] Seismic moment is converted to moment magnitude (M_w) after *Hanks and Kanamori* [1979]:

$$M_W = \frac{2}{3}\log_{10} M_O - 10.7 \quad (3)$$

[20] This relationship is used to plot the logarithm of the cumulative number of earthquakes above a certain magnitude as a function of magnitude for various regions and time intervals. We calculate the *b*-value and its uncertainty using the method outlined by *Wiemer and Wyss* [2002]. For a range of completeness magnitudes, this method determines the goodness of fit between the observed frequency-magnitude distribution and a synthetic distribution predicted by the maximum likelihood solution. The *b*-value is determined from the minimum completeness magnitude, M_C; we take the *b*-value that corresponds to either the maximum of the goodness of fit or the first instance that the goodness of fit exceeds 0.9. Uncertainties in

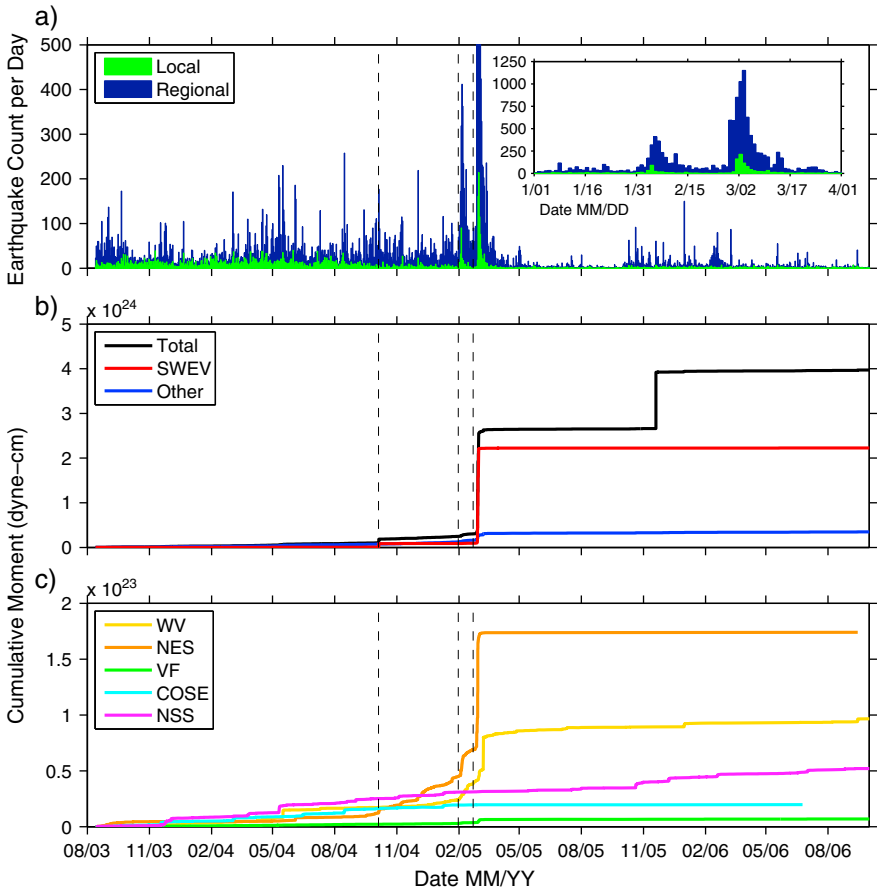

Figure 3. (a) Histogram of daily earthquake counts between August 2003 and October 2006. Local earthquakes located within 3 km of the nearest station are shaded green, while regional earthquakes located further away are shown in blue. Note that the maximum rate for the February 2005 swarm has been clipped at 500 events/day, but peak activity exceeds 1000 events/day. The dashed black lines show the onset times for the October 2004, January 2005, and February 2005 swarms discussed in the text. (b) The cumulative moment release rate for the entire catalog (black), SWEV (red), and for the five other regions combined. (c) Cumulative moment release rates for all regions except the SWEV.

b-value are calculated following the method of *Shi and Bolt* [1982].

5. Results

[21] Our catalog comprises 36,523 earthquakes occurring between August 2003 and October 2006 along the Endeavour Segment and adjacent segments (see supporting information for the full catalog). Figure 3a shows a histogram of daily earthquake counts of regional (epicenter >3 km from all stations) and local earthquakes. During the deployment, two seismic swarms in January and February 2005 ruptured the northern portion of Endeavour Segment and the adjacent southern extension of the West Valley Segment. Following the swarms, the average daily seismicity count decreases to ~12% of pre-swarm levels. Though the period between April and October 2005 is an interval of reduced network sensitivity due to two station failures and degraded data fidelity on two others (Table 1), the decrease is apparent at all magnitude thresholds. If we consider the period between October 2005 and June 2006 to be a better representation of post-swarm seismicity levels, the observed seismicity levels still decrease substantially to ~17% of pre-swarm levels.

[22] Figure 4 shows epicenters color coded by origin times relative to the 2005 swarms and outlines six seismically active regions which we will refer to as West Valley (WV) which also includes the area around the Endeavour and East Heck seamounts; Northern Endeavour Segment (NES) including the area to the east of the ridge, South-West Endeavour Valley (SWEV) including the area immediately north of the network, the Vent Fields (VF), the Cobb Overlapping spreading center and Southern Endeavour segment (COSE), and the Northern Symmetric Segment (NSS). Figure 3b shows the moment release for the full catalog. Except for a magnitude 5.4 earthquake on 19 November 2005 that is located in West Valley to the north of most of the seismicity in our catalog, nearly all the moment release occurs within the six geographic regions.

[23] Median formal location uncertainties for each region were calculated with *Hypoinverse* for subsets of earthquakes with at least 10 arrivals and are listed in Table 3. Within the network, the median maximum horizontal and median vertical uncertainties are 0.5 km and 0.8 km, respectively. Outside the network where the depth is fixed, the maximum 1-σ horizontal uncertainty tends to be tangential to the network and ranges from ~1 km in the southern portion of SWEV to 4–5 km at the segment ends. In the radial direction, the formal

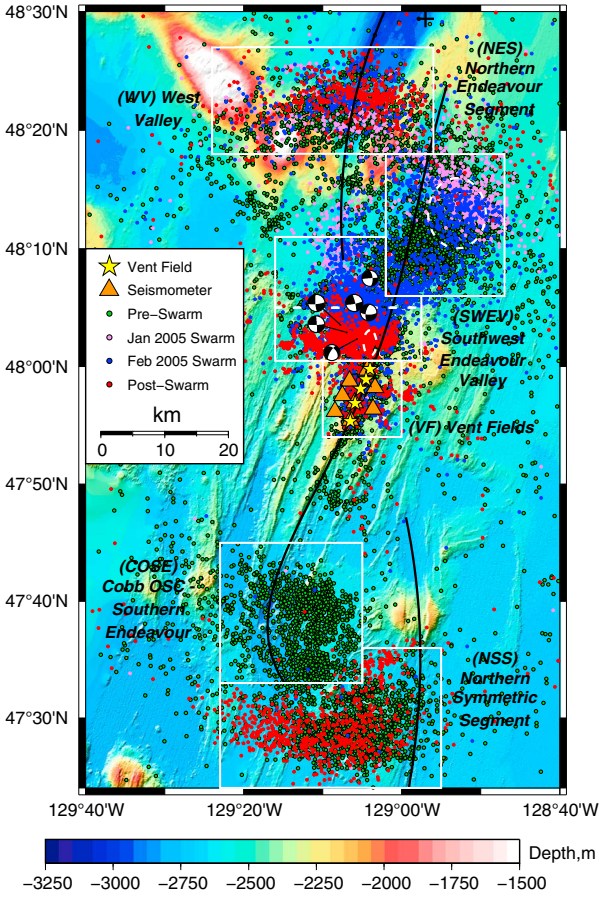

Figure 4. Segment-scale bathymetric map showing epicenters of 27,066 earthquakes located with at least eight total arrivals. Colors indicate the time periods prior to the 2005 swarms (green), during the January 2005 swarm (violet), during the February 2005 swarm (blue), and following the swarms (red). Dashed white ellipses indicate seismically active areas associated with the 5 October 2004 swarm. The labeled boxes show the six regions of seismicity discussed in the text. For the purpose of assessing location errors, the SWEV has been further subdivided by the white dashed line into northern and southern regions. Focal mechanisms are shown for six large earthquakes in the February 2005 swarm analyzed by the Canadian National Seismograph Network. A cross near the northern edge of the map shows the location of a magnitude 5.4 earthquake on 19 November 2005 that is apparent in the cumulative moment release curve for the catalog (Figure 3b). Note that seismic activity occurring earlier in the deployment, particularly the portion of the January 2005 swarm located within the SWEV, is partially obscured by the February 2005 swarm but can be seen in the animated version of this figure (see supplementary online material).

Table 3. Median Formal Location Uncertainties

Region	$\bar{R}$ (km)	L_{maj} (km)	AZ_{maj} (°N)	L_{min} (km)	AZ_{min} (°N)	L_{vert} (km)	$L_{VP/VS}$ (km)
WV	46	4.3	87	1.2	2	-	4.8
NES	32	3.3	116	1.1	27	-	3.2
Northern SWEV	18.7	1.8	113	1.0	11	-	2.0
Southern SWEV	11.2	1.0	143	0.7	59	-	1.3
VF	2.4	0.5	4	0.3	13	0.8	0.2
COSE	36.5	4.3	106	1.3	16	-	3.8
NSS	51.7	5.3	90	1.4	4	-	4.7

Earthquakes with at least 10 arrivals were used to calculate the median formal location uncertainties from *Hypoinverse* for each region shown in Figure 4, with the SWEV divided into northern and southern portions. $\bar{R}$ is the median distance to the events from station KEMO, L is the length of the major (L_{maj}) and minor (L_{min}) principle axis of the 1-σ error ellipse, while AZ is the azimuth of the principle axis, measured clockwise from North. Vertical uncertainties (L_{vert}) were only calculated for the VF earthquakes since the depth was fixed for events outside the network. $L_{VP/VS}$ are additional radial uncertainties that would arise from a 5% uncertainty in V_P/V_S.

horizontal location uncertainties are significantly smaller. However, these uncertainties do not include contributions from uncertainties in the ratio of V_P/V_S [*Hooft et al.*, 2010]. An uncertainty of 5% in V_P/V_S leads to an additional uncertainty in the radial direction that is ~12% of the distance to an event. As a result, total uncertainties in the radial and tangential directions are similar. It also should be noted that none of the uncertainties include the effect of systematic errors arising from crustal velocity heterogeneity which is quite significant in this region [*Weekly et al.*, 2011]. To first order, such errors will not affect the pattern of epicenters in a given region but they may substantially offset distant epicenters from their true location.

5.1. Northern Seismicity

[24] Figure 5 shows the distribution of epicenters, histograms of earthquake occurrence, moment release curves, and *b*-value plots for earthquakes to the north of the network in the WV, NES, and SWEV regions. To allow comparisons of moment release between regions, the moment release curves for each region are also shown in Figures 3b and 3c. The cumulative moment releases totaled 1×10^{23} dyne cm, 2×10^{23} dyne cm, and 2×10^{24} dyne cm for the WV, NES, and SWEV, respectively, with the majority of seismic energy released during the January and February 2005 swarms (Figures 3b and 3c). Prior to the 2005 swarms, the histograms of daily earthquake counts and the small step-like increases in the cumulative moment release rates (Figures 5b–5d) indicate that smaller swarms typically occurred every few months in each region, lasted 1–2 days, and comprised up to ~100 earthquakes (Figures 5b–5d). There were several swarms in WV between April and June 2004 (Figure 5b), a swarm in NES in June 2004 (Figure 5c) and another in SWEV and NES on 5 October 2004 that was large enough to be detected by SOSUS (http://www.pmel.noaa.gov/vents/acoustics/seismicity/nepac/endeav1004.html) (Figures 5b and 5c). Starting roughly coincident with this swarm on 5 October 2004, seismicity rates progressively ramp up over several months preceding the 2005 swarm sequences mainly in the WV and NES (Figures 5b and 5c).

[25] Figure 6 shows the distribution of epicenters for the 5 October 2004; January 2005 and February 2005 swarms color coded by time. The 5 October 2004 swarm (Figure 6a) includes ~250 earthquakes that occurred in two locations, the NES about 20–30 km north of the network and SWEV about 5 km north of the network. The net seismic moment release was 1.8×10^{22} dyne cm with 65% released in the NES. Seismicity commenced early on 5 October at both locations and lasted for 2 days with no resolved spatial migration of epicenters.

[26] The swarms in January and February 2005 included activity in multiple regions (Figures 6b and 6c). The January swarm lasted from 31 January to 13 February and included ~2000 earthquakes. The net seismic moment release was 4.0×10^{22} dyne cm with the NES, WV, and SWEV contributing 55%, 30%, and 15%, respectively (Figures 5b and 5d). At the swarm onset, earthquakes concentrated ~5 km west of the northern Endeavour Segment near Endeavour Seamount (Figure 6b). The rates of seismicity increased markedly on February 3, and the focus of earthquakes on the color-coded plot appears to move towards the southeast over 2–3 days. This is confirmed by a plot of earthquake longitude versus time (Figure 7a), which shows that location of the most intense seismicity, but not its onset, moved east at a rate of 0.4 km/hr. While there may be large systematic offsets in locations at this distance from the network, this temporal trend cannot be attributed to

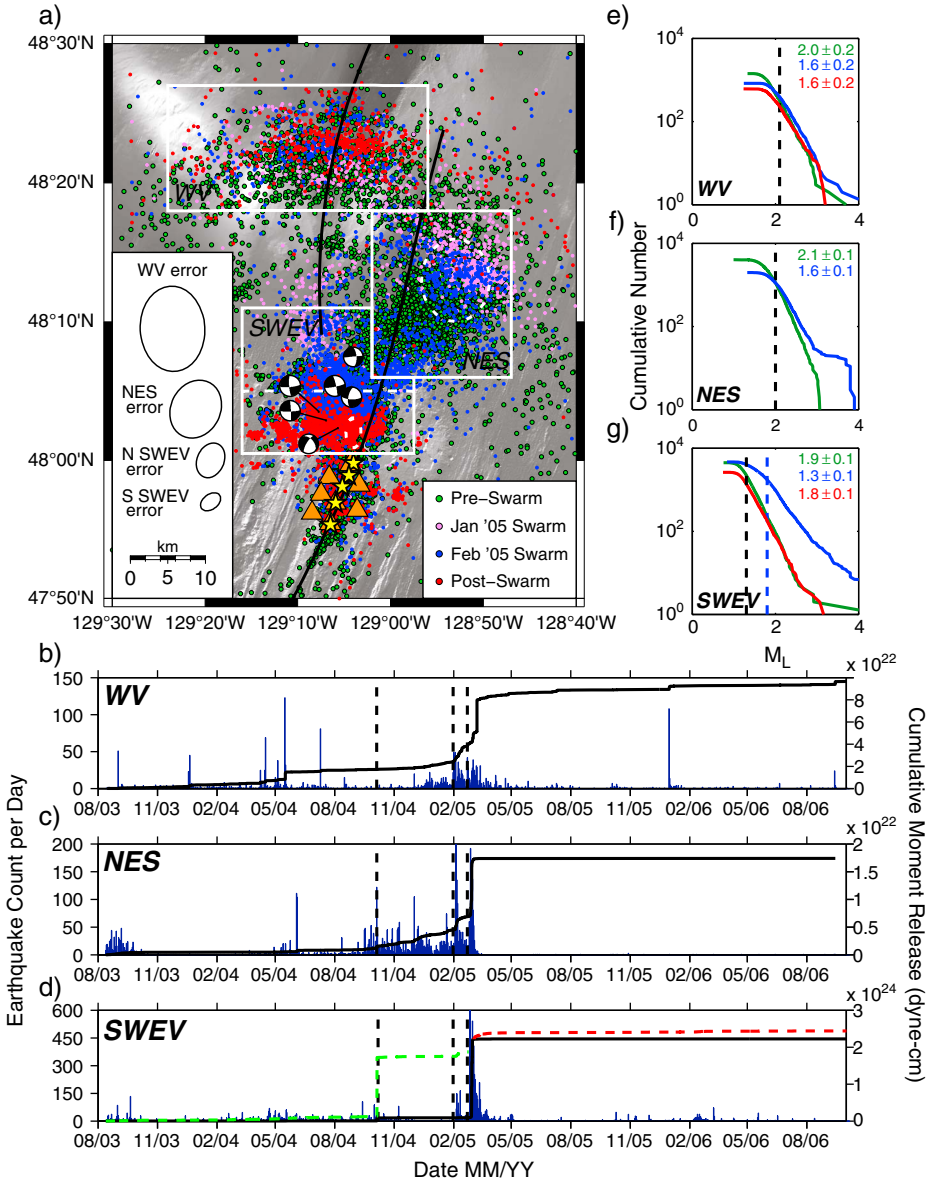

Figure 5. Seismicity within the northern regions. (a) Grayscale bathymetry overlain with earthquakes color coded as in Figure 4. Median 1-σ location uncertainty ellipses are shown for the WV, NES, and northern and southern portions of the SWEV region (delineated by a dashed white line) and include both formal location errors from *Hypoinverse* and an estimate of the uncertainty resulting from incomplete knowledge of the V_P/V_S ratio. (b–d) Histograms showing the daily counts of earthquakes and moment release curves for the (b) WV, (c) NES, and (d) SWEV. Note that different vertical scales are used for each plot. Vertical dashed lines show the onset times of the 5 October 2004 and January and February 2005 swarms. (e–g) Plots of earthquake count versus magnitude threshold for (e) WV, (f) NES, and (g) SWEV for the periods before (green), during (blue), and after (red) the 2005 swarms. The *b*-values and 2-σ uncertainties are labeled on the plots and dashed lines show magnitude of completeness. To directly compare *b*-values for pre-swarm and post-swarm periods, a single value for the magnitude of completeness was chosen (dashed black lines) while a separate magnitude of completeness was chosen to calculate *b*-value for the swarms (dashed blue line).

location error. Activity persisted in the NES and WV regions for the remainder of the swarm.

[27] Activity in SWEV on the southern extension of the West Valley Segment commenced on 5 February, 6 days after the swarm started (Figure 6b). Our catalog does not discern a clear migration direction for the initial epicenters in this region, although the locus of most intense seismicity jumped 5–10 km southward on 6 February (Figure 7b) where it was sustained within a ~5 km^2 area for the remainder of the swarm. On 11 February, an intense cluster of

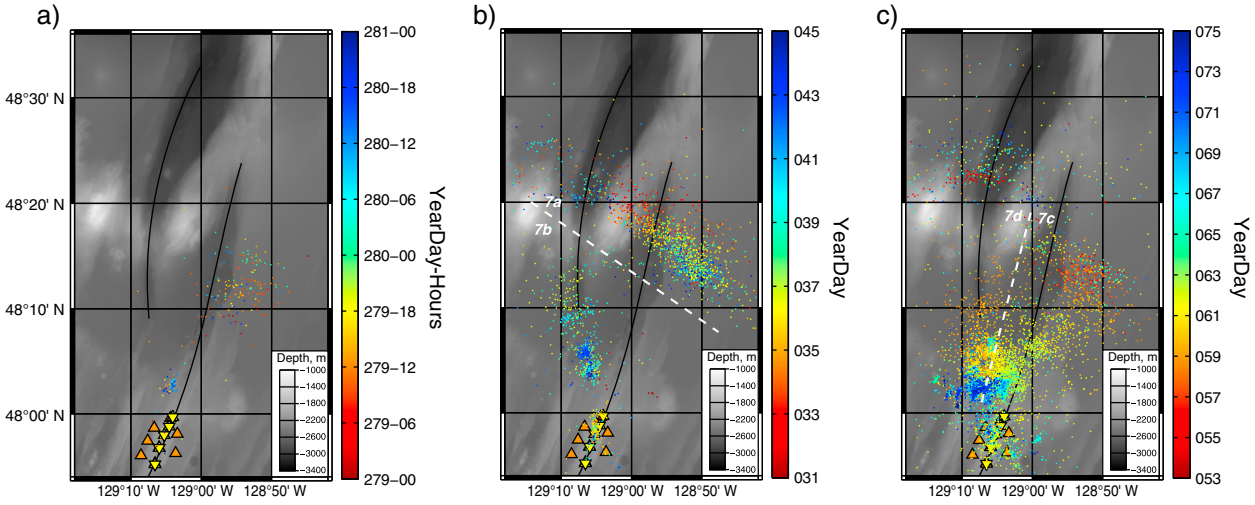

Figure 6. Gray scale bathymetric map showing epicenters (colored dots) located along the Endeavour and West Valley segments (solid black lines) during the (a) 5 October 2004, (b) January 2005, and (c) February 2005 swarms. The color of the epicenters indicates the calendar day as shown in the color bars; cooler colors show earthquakes that occurred later in the respective swarm. Note the difference in duration of each swarm. All earthquakes that satisfied our minimum location criteria of six arrivals are shown. White dashed lines delineate the regions used to analyze the migration patterns of earthquakes as shown in Figure 7.

earthquakes migrated about 2 km south over 12 h at 0.15 km/hr (Figure 7b).

[28] The second, larger February swarm occurred over ~23 days between 22 February and 16 March, and was first analyzed by *Hooft et al*. [2010]. While the earthquakes occurred in roughly the same regions as the January swarm, the seismicity patterns differ significantly. For this swarm, our catalog includes ~5000 earthquakes, and the total moment release was 2.3×10^{24} dyne cm with >90% released in the SWEV region (Figure 5c). Because earthquakes in the NES and SWEV merge for this swarm, we divide them for the purposes of the migration analysis using a boundary approximately midway between the Endeavour spreading axis and West Valley propagator (Figure 6c). The earliest seismic activity is located within the WV and NES (Figure 6c). Seismicity rates increased in NES on 25 February and spiked again on 27 February (Figure 7c), the onset of the main swarm as identified by *Hooft et al*. [2010]. Additional clusters of seismicity occurred progressively further southward on 28 February, 1 March, and 2 March (Figure 7c). Overall, the seismicity migrates about 20 km south at ~0.25 km/hr. If this seismicity is located on the Endeavour ridge axis, then the epicenters further to the north may be systematically offset ~10 km to the east.

[29] Earthquakes within the SWEV commenced ~6 h after the onset of the 27 February activity in NES. Our data show that the onset of SWEV seismicity migrated rapidly 20–25 km to the south over 10 h at a rate of 2 km/hr (Figure 7d) from the tip of the WV propagator toward the western abyssal ridge. On 28 February and 1 March, the six largest earthquakes occurred in this region. They have strike-slip focal mechanisms that require either right-lateral motion on N-S trending faults or left-lateral motion on E-W trending faults. Over several days, the focus of the most intense seismicity in the SWEV migrated ~10 km to the south and southeast where it merged with the southward migrating earthquakes on the NES around 3 March (Figure 6c). After 8 March, the epicenters appear to branch into several distinct north-south linear trends at latitudes between 48°04′N and 48°02′N with the easternmost earthquakes about 5 km north of the Sasquatch vent fields; this is also the area where the October 2004 SWEV activity was located (Figure 4).

[30] The rate of seismicity decayed steadily during the period 10–15 March. Following the end of the February swarm, seismicity in WV returns to pre-swarm levels and nearly ceases in NES (Figures 5a and 5b). In SWEV, seismicity continues at moment release rates that are about half the pre-October 2004 levels in an east-west band that extends from the ridge axis a few kilometers north of the network to about 15 km to the west (Figure 4).

[31] For WV, SWEV, and NES, pre-swarm *b*-values (Figures 6e–6g) are similar for all three regions (~2). During the January and February 2005 swarms, the *b*-values for the WV and NES regions decrease

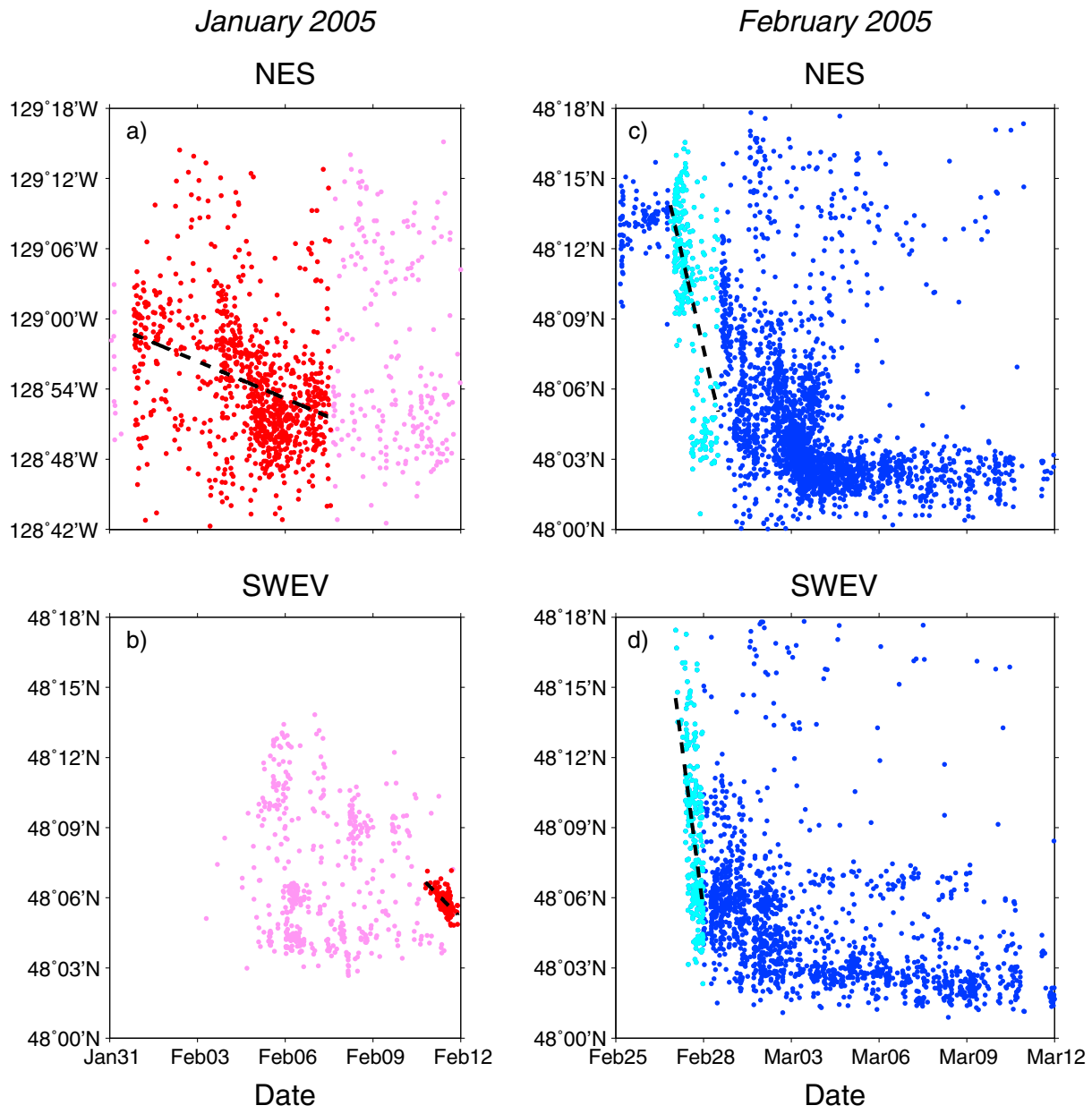

Figure 7. Plots showing the temporal migration of earthquakes in the 2005 swarms. (a) Longitude versus time for earthquakes on the northern Endeavour in the January swarm. (b) Latitude versus time for earthquakes on West Valley propagator in the January swarm. (c and d) Latitude versus time for earthquakes on northern Endeavour and West Valley propagator, respectively, in the February swarm. The division of earthquakes between geographic regions is illustrated in Figure 6. Dashed lines indicate the linear fit calculated by fitting a least squares straight line to specific time segments (indicated by color highlighting).

moderately to a value of 1.6, while the SWEV *b*-value decreases substantially to 1.2. The *b*-value for WV remained at a value of 1.6 while the *b*-value for SWEV rebounded to 1.9, comparable to the pre-swarm value. We were unable to calculate a post-swarm *b*-value for the NES region since very few earthquakes were located in the region during this time.

5.2. Vent Field Seismicity

[32] The cumulative moment release in the VF region is 6.9×10^{21} dyne cm, substantially lower than in other regions (Figure 3c). Between August 2003 and September 2004, we located an average of nine events/day, all with magnitudes less than ~2.5. The most intense seismic activity (Figure 8a) is between the High Rise and Main Endeavour fields extending

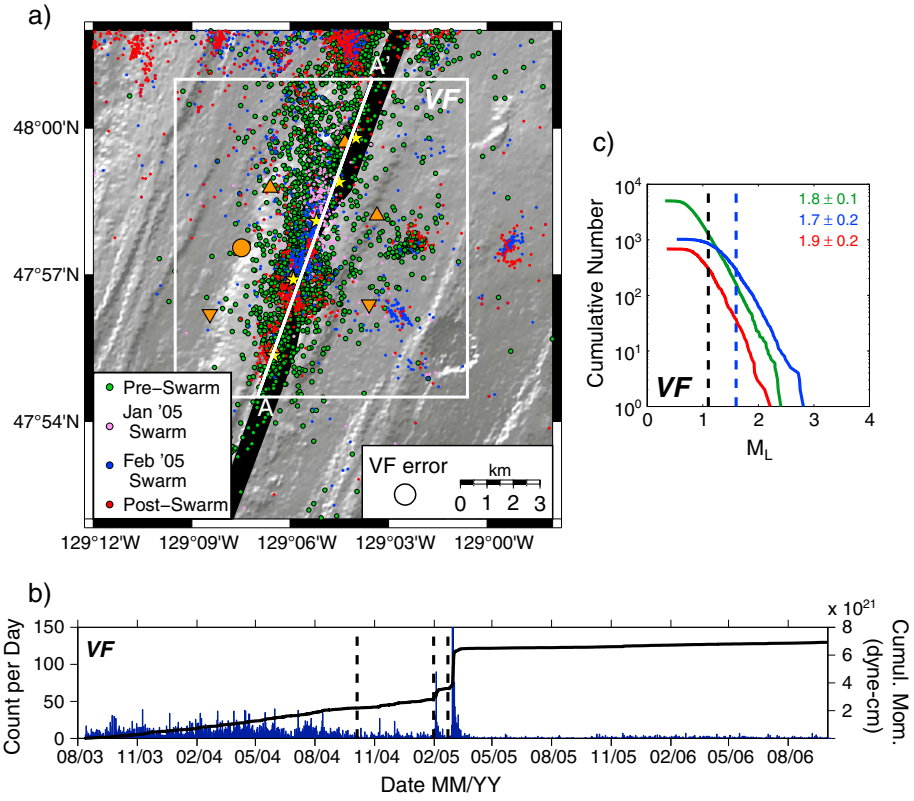

Figure 8. Seismicity in the Vent Field region plotted using the same conventions as Figure 5. (a) Bathymetric map of vent field area showing all earthquakes located with at least six arrivals color coded by time. High-temperature vent fields (yellow stars), seismometers (orange symbols), and the footprint of the AMC (gray shadow) are also shown. The white line (A-A′) shows the location of the along-axis cross section in Figure 9. (b) Histogram of daily earthquake counts and moment release curve with the onset of the swarms shown by dashed black lines. (c) Plot of earthquake count versus magnitude threshold used to calculate *b*-values and 2-σ uncertainties for periods before (green), during (blue), and after (red) the 2005 swarms. Note that a different magnitude of completeness was used to calculate *b*-values for the swarm period (dashed blue line) than for the periods before and after (dashed black line) the swarms.

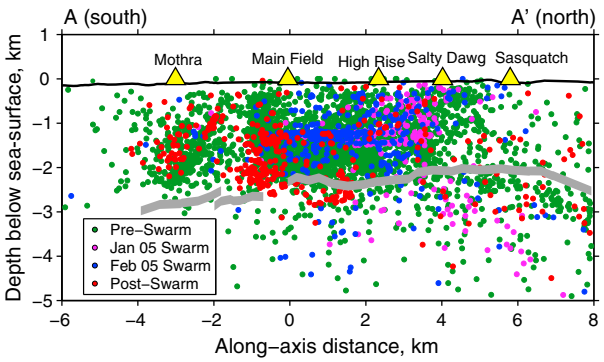

Figure 9. Along-axis cross section showing vent field earthquakes for different time periods (circles color coded by time as in Figure 4). The thick gray line shows the top of the AMC [*Van Ark et al.*, 2007]. The location of the cross section is shown in Figure 8, and the maximum horizontal projection distance is 1 km.

up to 1 km south of the Main Endeavour field with a smaller cluster of seismicity near Mothra field. The depths of VF earthquakes (Figure 9) are consistent with a ~1 km thick band of seismicity directly overlying the AMC [*Tolstoy*, 2008a; *Wilcock et al.*, 2002; *Wilcock et al.*, 2009].

[33] The rate of seismicity decreased by 60% during fall 2004 (Figure 8b), approximately a month prior to the 5 October swarm in NES and SWEV. During the January and February 2005 swarms, seismicity within the VF region increased starting 1–2 days after the swarm onsets (Figures 5d and 8b). Peak daily seismicity counts are ~100 and ~200 events/day for the January and February swarms, respectively. The swarms account for about 50% of the total moment release in the region and include earthquakes with magnitudes up to 2.8. Seismicity during the January swarm located primarily between the High Rise

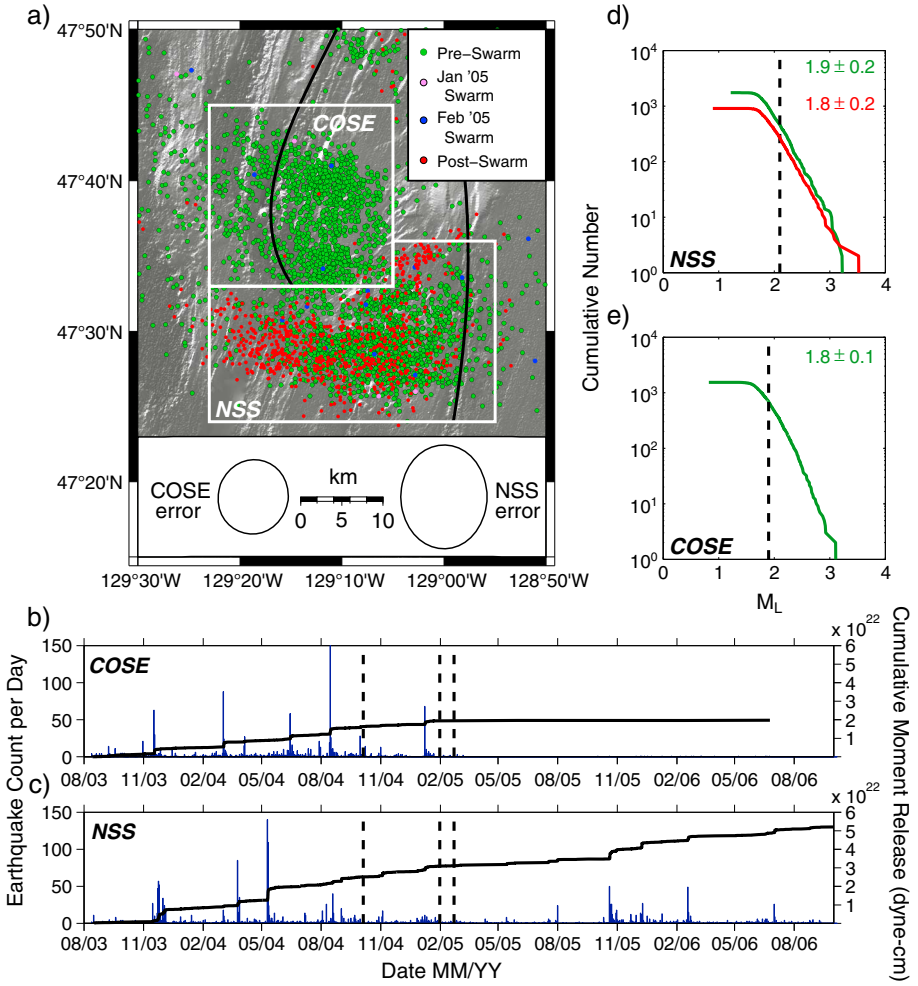

Figure 10. Seismicity in the southern regions plotted using the same conventions as Figures 5 and 8. (a) Grayscale bathymetry overlain by epicenters color coded by time. (b and c) Histograms of daily earthquake counts and moment release plots for the (b) COSE and NSS regions with the onset of the 2005 swarms shown with dashed black lines. (d and e) Plots of earthquake count versus magnitude threshold used to calculate *b*-values. The *b*-values and their uncertainties are labeled on the plots with dashed lines showing the magnitude of completeness. No *b*-values were calculated for the swarm periods, or for the post-swarm COSE region, because of an insufficient number of earthquakes.

and Salty Dawg fields, while earthquakes were concentrated farther south between the Main Endeavour and High Rise fields during the February swarm (Figures 8 and 9). During the swarms, the earthquakes also tend to locate at shallower depths (Figure 9). Because the network was significantly degraded during the swarms (Table 1) and in our experience *Hypoinverse* sometimes preferentially locates earthquakes near particular layer interfaces, the clustering of locations near 1.2 km depth may be an artifact of the location algorithm.

[34] Following the swarms, the rate of seismicity decreased to ~15% of pre-swarm values and maximum earthquake magnitudes were ~2.2. The highest concentration of earthquakes is to the south of the Main Endeavour field with additional clusters between High Rise and Main Endeavour and near Mothra, similar to pre-swarm patterns (Figure 8a). Seismic *b*-values within the region were 1.7 both before and after the swarms, dropping to 1.4 during the swarms (Figure 8c).

5.3. Southern Seismicity

[35] Seismicity located south of the Keck network (Figure 10a) was primarily associated with deformation in the Cobb OSC (COSE) and on the Northern Symmetric Segment (NSS). The cumulative seismic moment release for the COSE and NSS totaled 1.9×10^{22} and 5.2×10^{22} dyne cm, respectively. Swarms lead to a step-like pattern of observed moment release because a large number of earthquakes are recorded within a short amount of

time (Figures 10b and 10c). There is an indication that there may be large systematic location errors due to velocity heterogeneity; if earthquakes on the NSS are centered on the spreading center, the COSE and NSS earthquakes may be mislocated on average 10–15 km too far west.

[36] Prior to the 2005 swarms, the average rate of seismicity in each region was 3–4 events/day. Following the swarms, the earthquake rates in NSS were unchanged, but the COSE region entered a sustained period of seismic quiescence with only a handful of earthquakes located over 18 months (Figure 10b). Thus, while seismicity on the south Endeavour segment almost ceased, the Northern Symmetric Segment was unaffected. The *b*-values in the two regions were ~2 before the swarm and do not change significantly in the NSS afterwards.

6. Discussion

6.1. The 2005 Swarms

[37] A key question for understanding the January and February 2005 swarms is the relative roles of tectonic and volcanic processes. The swarms exhibited complicated rupture patterns with seismicity occurring throughout a broad region encompassing the WV, SWEV, NES, and VF regions (Figures 6b and 6c) and appear to be closely linked based on the similar distributions of seismicity along the northern Endeavour segment and the southern extension of the West Valley segment. The seismic moment release of the February swarm is nearly 2 orders of magnitude larger than the January swarm. However, the magnitude of the pressure anomalies measured at regional boreholes shows that the majority of the moment release was aseismic [*Hooft et al.*, 2010]; the pressure anomalies associated with the February swarm are only about twice those for the January swarm suggesting that the aseismic moment releases are more similar (E.E. Davis, personal communication). The borehole pressure data [*Hooft et al.*, 2010] and some of the characteristics of seismicity including the lack of main shocks, *b*-values that are always significantly greater than unity, and the migration of epicenters are consistent with a magmatic swarm. However, other characteristics such as the band of epicenters striking oblique to the northern Endeavour during the January 2005 swarm, the strike-slip focal mechanisms within the Endeavour-West Valley OSC during the January 2005 swarm and the decrease in *b*-values observed in several regions are difficult to attribute to magmatic processes and suggest a tectonic component.

[38] The onset of the January swarm on 31 January is marked by earthquakes in the Endeavour-West Valley OSC near the vicinity of Endeavour Seamount. Over 2–3 days, epicenters in the NES region migrated 20 km southeast along a trend oblique to the Endeavour ridge (Figure 6b). Although this trend appears to extend well east of the ridge axis onto the Juan de Fuca plate, the epicenters in this region may be systematically displaced to the east. The curious migration pattern does not correlate with any trends in seafloor morphology and is inconsistent with propagation of a dike along the northern Endeavour Segment. One explanation is that the trend could be due to shear deformation associated with reorganization of the Pacific-Juan de Fuca-Explorer plate boundary. Specifically, from an analysis of regional bathymetry, the distribution of epicenters from SOSUS and focal mechanisms from the Canadian National Seismograph Network, *Dziak* [2006] argues that the Heck, Heckle and possibly Springfield seamount chains overlie splays of a broad southward migrating Sovanco transform fault that provide conduits for seafloor volcanism. The earthquakes we observe align with the eastward extension of the Heck seamount chain and could indicate strike-slip motion along this splay.

[39] Seismicity in the SWEV initiated 4 days after the NES on 5 February. The epicenters extend ~15 km along the N-S trend of the West Valley propagator with most of the seismicity concentrated at the southern end of the Endeavour Valley (Figure 6b) well to the south of the bathymetric expression of the propagator. No clear along-axis migration of epicenters is resolved (Figure 7b) except for a short episode of seismicity near the end of the swarm. Thus, the earthquake epicenters alone do not provide conclusive evidence for a volcanic source. However, for this swarm, the borehole pressure data (E.E. Davis, personal communication) suggest that nearly all the moment release is aseismic and the characteristics of the pressure anomalies require a coseismic strain that was substantially different from the June 1999 [*Davis et al.*, 2001] and February 2005 swarms [*Hooft et al.*, 2010]. Rather than decreasing, the pressures to the north in Middle Valley increased indicating reduced pore volume. On the western ridge flanks, the pressures also increased but the relative amplitude was markedly less than for the other swarms. This pattern of pressure anomalies may be compatible with the injection of a northwest-

southeast oriented dike near the southern tip of the West Valley Segment (E.E. Davis, personal communication). Southward growth of the West Valley propagator beyond the region in which it has a bathymetric expression is consistent with models for the evolution of the Endeavour-West Valley OSC that predict the eventual truncation of the Endeavour Segment [*Karsten et al*., 1990].

[40] The February swarm was analyzed previously by *Hooft et al*. [2010]. Although the majority of the seismic moment release was within the SWEV region, the swarm initiated in the NES. From the pattern and timing of borehole pressure anomalies and their similarity to the 1999 swarm, *Hooft et al*. [2010] infer the swarm was linked to a dike injection on the NES. We locate the NES earthquakes significantly to the east of the spreading axis, but the locations may be biased by large velocity heterogeneities within the region [*Weekly et al*., 2011]. *Hooft et al*. [2010] did not resolve migration of the onset of seismicity in the NES but found that the seismicity switched off from north to south. Unlike *Hooft et al*. [2010] who subdivided the earthquakes into rectangular regions similar to those shown in Figure 4, we subdivide the earthquakes in the February swarm by their proximity to the Endeavour segment and the West Valley propagator (Figure 6c). We find that the earthquakes closest to the Endeavour segment are concentrated in bursts that migrate unsteadily 30 km south over about 3 days (Figure 7c). This migration of earthquakes supports the inference that the February swarm was associated with a dike on the NES [*Hooft et al*., 2010] although it suggests that the pattern of injection was complex. The overall migration rate is lower than observed for eruptive events [*Dziak et al*., 2007]. The north to south migration direction is inconsistent with a dike sourced from the AMC associated with the elevated central portion of the Endeavour Segment [*Van Ark et al*., 2007] and could be interpreted as evidence of a tectonic cause. Alternatively, a southward propagating diking event on the northern Endeavour could have been sourced from the north by magma associated with the Heck Seamounts [*Dziak*, 2006] and specifically the Endeavour Seamount, which lies at the northern end of the Endeavour-West Valley OSC (Figure 1). For this interpretation, one can speculate that the southeast striking band of epicenters in the January swarm may have been associated with fault-controlled melt supply from the Endeavour Seamount to the northern Endeavour segment.

[41] *Hooft et al*. [2010] resolved a southward migration of epicenters on the SWEV starting 11 h after the initiation of the main swarm on the NES on February 11. Using our division of earthquakes, we find that seismicity on the West Valley propagator initiates about 6 h after the NES, somewhat earlier than reported by *Hooft et al*. [2010]. The onset of seismicity migrates ~20 km south at about 2 km/hr (Figure 7d), much faster than the speed of ~0.6 km/hr reported by *Hooft et al*. [2010]. This migration rate is consistent with observations for eruptive diking events at mid-ocean ridges [*Dziak et al*., 2007], but an event response cruise found no evidence for an eruption (http://www.pmel.noaa.gov/vents/acoustics/seismicity/nepac/endeav0205/response-cruise.html). *Hooft et al*. [2010] argue that the borehole pressure data are inconsistent with a strain field created by a northwest-southeast oriented dike in the SWEV. However, this inference does not preclude a diking event on the West Valley propagator but rather requires that the pressure signal be dominated by a larger event on the northern Endeavour segment.

[42] The six largest events of the swarm occurred in SWEV on 28 February and 1 March and the swarm continued in this region for about 2 weeks. The presence of large earthquakes is reflected in the low *b*-value of 1.3 observed during the swarm in this region (Figure 5g) and suggests an enhanced tectonic component. However, it is important to note that the focal mechanisms indicate a sense of strike-slip motion on ridge-perpendicular faults that is opposite to the offset of the OSC. *Hooft et al*. [2010] argue that these mechanisms might reflect reactivation of ridge-parallel strike-slip faults in the OSC in response to the stress changes induced by a dike intrusion on the northern Endeavour. During the second week, seismicity reached the southern end of the SWEV region (~48°02′N) and earthquakes appear to cluster into several distinct north-south lineations spaced 2–3 km apart that may correlate with seafloor topographic features. The slow epicentral migration to the south and southeast, oscillatory seismic rate [*Hooft et al*., 2010], lack of aftershock activity, and a possible correlation to seafloor volcanic features suggests that this seismicity could be associated with magma bodies that extend across the OSC as observed on the East Pacific Rise at 9°03′N [*Kent et al*., 2000; *Toomey et al*., 2007]. The restoration of high *b*-values in the SWEV region following the swarm (Figure 5g) is consistent with a volcanic influence. Alternatively, the observation that the SWEV region remains seismically

active following the 2005 swarms (Figure 4) could be interpreted and indicative of a tectonic response to static stress changes.

[43] In summary, the dominant signal in the borehole pressure records is a diking event on the northern Endeavour in late February [*Hooft et al*., 2010] which we infer extends 20 km along axis from 48°15′N to 48°02′N (Figure 8c). The origin of the seismicity that trends oblique to the NES in the earlier January swarm is enigmatic, and the interpretation of magma migration from under Endeavour Seamount is speculative. We infer that both swarms also involved intrusions beyond the tip of the West Valley propagator and that there was possibly additional magmatic activity elsewhere in the Endeavour Valley near the conclusion of the February swarm. The drop in *b*-values during the swarm, particularly in the SWEV region (Figure 5g), is surprising given the evidence for magmatic extension and suggests a tectonic component. Focal mechanisms of larger events determined from land-based networks (Figures 4 and 5) indicate east-west strike-slip motion, which is counter to the offset of the OSC.

[44] We interpret the 2005 swarms as the terminus of a 6 year spreading episode that started in 1999 and ruptured the Endeavour Segment. The 1999–2000 swarm sequence extended along the central and southern portions of the Endeavour segment from about 47°40′N to 48°05′N [*Bohnenstiehl et al*., 2004]. The 1999 swarm was interpreted in terms of a 40 km long dike [*Davis et al*., 2001] and the characteristics of earthquakes in the 2000 swarm are consistent with a deeper intrusion although a tectonic cause is also possible [*Bohnenstiehl et al*., 2004]. The combination of diking events in 1999, 2005 and possibly 2000 appears to have ruptured the majority of the Endeavour segment from about 47°40′N to 48°15′N. Following the February 2005 swarm, seismicity essentially ceased at the ends of the segment and decreased substantially in SWEV and VF regions (Figure 4) suggesting that extensional stresses have been relieved along the entire segment.

6.2. Comparison With Other Magmatic Spreading Events

[45] SOSUS monitoring has provided a 20 year record of seismic swarms on the Juan de Fuca and Gorda ridge including those associated with eruptive (1993 on CoAxial [*Dziak et al*., 1995], 1996 on the Gorda Ridge [*Fox and Dziak*, 1998], and 1998 on Axial Seamount [*Dziak and Fox*, 1999a]) as well as many non-eruptive spreading events. A synthesis of the observations [*Dziak et al*., 2007] suggests that eruptive events are characterized by an early onset of earthquake migration and faster migration rates. It is thought that higher excess magma pressure is required for eruptions, most likely because of magma recharge into crustal magma bodies prior to the eruption. At the detection threshold of SOSUS, the February 2005 Endeavour swarm fits this model; the speed of migration of 0.2 km/hr and onset after 72 h compare with speeds of 1–2 km/hr and onset times <1 day for the eruptive events [*Dziak et al*., 2007]. However, our local network data present a more nuanced picture. In the presence of substantial precursory activity, the onset time of a swarm is somewhat subjective. While earthquakes on the northern Endeavour only migrate southward at 0.25 km/hr, there is fast migration at ~2km/hr on the West Valley propagator (Figure 7d) within hours of the onset of the main swarm.

[46] From a theoretical standpoint, it is not clear why eruptive and intrusive diking events should always have distinct seismic characteristics. *Buck et al*. [1997] explain the difference between eruptive and non-eruptive events in terms of the relative values of the overburden pressure at the AMC and the pressure at the base of a column of erupting magma. In this model, the thickness of low-density extrusives at any particular site will be self-regulating so that the average density of the upper crust matches that of the least dense erupting lavas. The difference between eruptive and non-eruptive events may reflect small changes in the composition and volatile content of the magma and in average upper crustal densities rather than profound difference in characteristics of dike intrusion.

[47] In comparison with the eruptive events observed along the Juan de Fuca ridge, the pattern of seismicity for the 2005 Endeavour swarm is complex. The three diking-eruptive events [*Dziak and Fox*, 1999a; *Dziak et al*., 1995; *Fox and Dziak*, 1998] were all characterized by seismicity focused in a single region that migrated down the gradient of the axial rift bathymetry on a timescale of ~2 days before decaying over several weeks. The duration of the two 2005 Endeavour swarms is similar, but seismicity was detected in four regions. This complexity partly reflects the improved resolution of a local seismic network compared to SOSUS (most of the SOSUS locations for the February 2005 swarm were in SWEV [*Hooft et al*., 2010]), but it also reflects the tectonics of the region and

in particular the involvement of two limbs of the OSC. It is interesting to note that the 1999 Endeavour swarm on the central/southern Endeavour led to seismicity on Surveyor Volcano on the Northern Symmetric Segment, the opposing limb of the Cobb OSC. *Bohnenstiehl et al*. [2004] inferred that dynamic stresses triggered earthquakes on the opposing limb of the OSC.

[48] The February 2005 swarm is unique in that the inferred dike on the northern Endeavour migrates up the gradient of the axial valley towards the center of the segment. This differs from the three eruptive events and the non-eruptive events on the Endeavour in 1999 [*Bohnenstiehl et al*., 2004] and Middle Valley in 2001 [*Davis et al*., 2004]. It is also different from the magmatic diking sequences observed on land at Krafla from 1974 to 1984 [*Sigmundsson*, 2006] and in Afar from 2005 to 2009 [*Ebinger et al*., 2010] which were both fed from a central magma body. This suggests that the source of magma for volcanism on Endeavour is more complex than the commonly accepted model in which magma is supplied to the crust at the center of the segment and the dikes migrate away from this source to the segment ends [e.g., *Macdonald*, 1998]. Given the presence of a large seamount in the Endeavour-West Valley OSC, it is plausible that the northern portion of the Endeavour segment might tap an alternate magma source. *Grandin et al*. [2012] argue that along-axis variations in the depth to the brittle-ductile transition play a greater role than topography in horizontal dike propagation because thicker lithosphere can store more elastic strain energy. If the 1999/2000 events on the central/southern Endeavour depleted a magma reservoir at the center of the segment, the elastic potential energy stored in the crust to the north may have drawn magma from an alternative source.

[49] If the 1999–2005 swarm sequence is considered as the magmatic phase of a single spreading cycle that ruptured the whole Endeavour segment, then the duration of the magmatic phase is substantially longer than other ridge-spreading events. The three eruptive events in the NE Pacific [*Dziak and Fox*, 1999a; *Dziak et al*., 1995; *Fox and Dziak*, 1998] were limited to single eruptions lasting for days. On the East Pacific Rise at 9°50′N, isotopic dating of lava flows suggests that the eruptions in 1991 and 2005 extended over ~1 year [*Rubin et al*., 1994] and ~6 months [*Rubin*, 2012], respectively. The timescales of the Endeavour event are more consistent with the observation of rifting on land where rifting episodes at Krafla Volcano, Iceland, and in Afar have lasted a decade and involve many dike intrusions along the same segment [*Ebinger et al*., 2010; *Sigmundsson*, 2006]. These sequences can be explained in terms of the large extensional stresses required to rupture thick lithosphere; the resulting large extensional strains coupled with a limited crustal magma reservoir requires multiple diking episodes with magma recharge of the magma body in between to accommodate the strain [*Qin and Buck*, 2008]. At the Endeavour, the lithosphere is thin and each portion of the ridge experienced only one major dike injection, but the interval between the 1999 and 2005 events may well reflect a timescale of magma supply. The sharp drop off in seismicity following the 2005 swarms is consistent with observations on Axial Seamount [*Dziak and Fox*, 1999b] and the East Pacific Rise [*Tolstoy et al*., 2006], which show a progressive ramp up in seismicity prior to eruptive events and a sharp decrease at their conclusion.

6.3. Precursory Activity and Triggering

[50] The patterns of seismicity surrounding the 2005 Endeavour swarms suggest seismic triggering over length scales from <10 km to 50 km and at various timescales. During the swarms, the seismicity migrated between regions on timescales of hours to days. The long-term decrease in seismicity along the Endeavour Segment following the 2005 swarms occurred within days or at most weeks. The spatial coincidence of earthquakes suggests that seismicity is linked between the two swarms on a timescale of 1 month. On a time scale of several months, the moment release rate in WV and NES gradually increases prior to the 2005 swarms starting with a small swarm on 5 October 2004. Finally, on a 6 year timescale, we infer that the 2005 swarms are linked to the 1999 and 2000 swarms that ruptured the Endeavour segment further south [*Bohnenstiehl et al*., 2004].

[51] Two mechanisms are invoked to explain remote earthquake triggering: coseismic changes to static Coulomb stresses [*Hardebeck et al*., 1998; *Harris and Simpson*, 1992; *King et al*., 1994; *Nostro et al*., 1997; *Stein et al*., 1997] and dynamic transient stresses induced by passing seismic waves [*Brodsky and Prejean*, 2005; *Gomberg et al*., 2001; *Hill et al*., 1993; *Kilb et al*., 2000; *Prejean et al*., 2004]. Static stress changes can either promote or retard seismic activity and operate over length scales of approximately three fault (or dike) lengths [*King et al*., 1994] and timescales that can be quite long [*Freed*, 2005]. Dynamic triggering can operate over longer ranges but on short timescales. Surface waves from earthquakes located up to several thousand kilometers away have triggered increases in

local seismicity in volcanic-hydrothermal systems on land [*Hill et al*., 1993; *Prejean et al*., 2004].

[52] On the Endeavour Segment, *Bohnenstiehl et al*. [2004] argued that dynamic triggering during volcanic intrusive events plays a role in triggering seismicity at other locations on the ridge. While we cannot discount this interpretation, we argue that static triggering could account for all the observations around for the 2005 swarms. To evaluate the feasibility of static triggering, it is necessary to know the pattern of deformation to determine whether regions of increased and decreased seismicity are consistent with the changes in the stress field from earlier events. Unfortunately, we do not know the detailed strain field associated with 2005 swarms, so it is not possible to quantify how static stresses linked active regions during the 2005 swarms. *Bohnenstiehl et al*. [2004] showed that the injection of the 1999 dike on the central Endeavour generated static stresses that reduced extensional stresses to either side but promoted extensional failure on the ridge axis to the south where the 2000 swarm occurred. The 1999 dike would also have generated extensional stresses on the ridge axis to the north that are consistent with the deformation inferred for NES in the February 2005 swarm [*Hooft et al*., 2010].

[53] A variety of post-seismic static stress transfer mechanisms can potentially explain the delay in triggered seismicity observed in our dataset. Viscoelastic relaxation involves transfer of elastic strain from the ductile lower crust and upper mantle to the brittle seismogenic upper crust. The characteristic timescale for the relaxation of a Maxwell solid is $2\mu/E$ where μ is the dynamic viscosity and E is Young's modulus [e.g., *Turcotte and Schubert*, 2002]. For an effective μ ranging from 10^{19} to 10^{21} Pa s and $E = 10^{11}$ Pa, the characteristic times are ~ 1 to 100 years. Detailed modeling shows that the relaxation times are dependent on the vertical viscosity structure, the depth of brittle-ductile transition, the dip angle of the fault, and the effective coefficient of fault friction [*Freed*, 2005; *Freed and Lin*, 1998; *Nostro et al*., 2001]. *Freed and Lin* [2001] show that the 7 year delay between the 1992 Landers and 1999 Hector Mine earthquakes is consistent with lower crustal and upper mantle viscosities of 1.6×10^{19} Pa s and 8×10^{18} Pa s, respectively. Beneath mid-ocean ridges, upper mantle viscosities are commonly modeled as 10^{18}–10^{19} Pa s [*Parmentier and Phipps Morgan*, 1990] but may either be higher at shallow depths due to dewatering [*Hirth and Kohlstedt*, 1996] or lower due to the presence of partial melt. The viscosities of hot and possibly partially molten lower crustal rocks are not well known, but experimental constraints suggest values similar to the mantle [*Hirth et al*., 1998]. Detailed modeling would be necessary to fully evaluate the timescales of viscoelastic relaxation in a mid-ocean ridge setting, but it is clearly a plausible mechanism to explain the time delay between the 1999–2000 swarms and the 2005 swarms.

[54] Poroelastic rebound occurs when the full static stress changes are not realized until pore fluids diffuse out of and into regions that experience volumetric compression and dilation respectively. The characteristic timescale for this process is given by D^2/η where D is the length scale and η the diffusion coefficient given by $\eta = k/\mu S$ with k the permeability, μ the fluid viscosity, and S the uniaxial storage compressibility [e.g., *Crone et al*., 2010]. *Hooft et al*. [2010] model the increase in vent field seismicity observed ~2.5 days following the onset of the February 2005 swarm on the northern Endeavour in terms of along-axis diffusion of a hydrologic pressure perturbation. Using a characteristic diffusion length and time of 35 km and 2.5 days, respectively, they estimate a crustal permeability $\sim 10^{-9}$ m^2. This value is high but consistent with permeability estimates for a sediment-capped layer 2A off axis [*Davis et al*., 2000]. Since there is no sediment cap on the ridge axis, pore fluid pressure perturbations are more likely to dissipate by vertical diffusion across the seafloor. The relatively shallow depths observed for the vent field seismicity during the swarms (Figure 9) are consistent with such an interpretation. Assuming the model parameters of *Crone et al*. [2010], reducing the diffusion length scale to 2 km yields a permeability of order 10^{-13} m^2 to 10^{-12} m^2 which matches estimates for ridge-axis hydrothermal fields [*Crone et al*., 2011; *Lowell and Germanovich*, 1994; *Stroup et al*., 2009; *Wilcock and McNabb*, 1996].

[55] When evaluating whether poroelastic rebound can account for triggering timescales in our data, it is important to recognize that the permeability of ocean crust can vary by many orders of magnitude [e.g., *Fisher*, 1998] and that the partial sediment cover in the region may lead to variations in the diffusion length scales. If permeabilities range from 10^{-14} m^2 to 10^{-10} m^2 and the diffusion length scale from 2 to 10 km, the timescales obtained from the model of *Crone et al*. [2010] will range from ~1 h to ~1 year. Given the wide range of feasible time scales, poroelastic

rebound could explain large portion of our triggering observations.

[56] Another mechanism that could account for a delay in triggering is the time required for pressure perturbations associated with the withdrawal or supply of magma to diffuse within and between magma systems. *Hooft et al*. [2010] argue that the characteristic diffusion timescale for a pressure perturbation within the axial melt/partial mush zone would exceed the timescales for poroelastic diffusion because of the higher viscosity of the magma. However, this inference may be incorrect because magma may be less compressible than water [e.g., *Spera*, 2000] and the effective permeability of the melt region is unknown. Indeed, if magmatic pressure reductions are the cause of decreased seismicity following the 2005 swarm, the short timescale for the segment-wide cutoff might be cited as evidence for a magmatic system that is well connected along axis, either within the crustal AMC and mush zone or below the Moho where the melt fractions may be high [*Dunn et al*., 2000].

7. Conclusions

[57] In this paper, we have presented a catalog of seismicity on the Endeavour Segment from 2003 to 2006 that is derived from a local seismic network. The primary conclusions are as follows:

- Two regional seismic swarms, beginning in January and February 2005, were observed along the northern portion of the Endeavour Segment and within the adjacent Endeavour Valley. While they appear to have a tectonic component, we infer that these events were linked to intrusive volcanism, including diking on the Northern Endeavour during the February swarm and smaller dike intrusions on the propagating tip of the West Valley segment during both swarms.
- The seismicity associated with the 2005 swarms is more complex than that of other documented mid-ocean ridge-spreading events. This likely reflects the complicated tectonics of the region and in particular the partition of magmatic spreading between two limbs of the Endeavour-West Valley OSC. The inference of a southward propagating dike on the northern Endeavour suggests that magma supply to the Endeavour may not be limited to the central portion of the segment and could be associated with the Endeavour seamount melt source.
- Following the February 2005 swarm, the average seismicity rate along the Endeavour Segment decreased substantially with seismicity almost ceasing entirely at the ends of the segment. Seismic rates on the overlapping portions of the adjacent segments did not change. We infer that the swarms of January and February 2005 mark the termination of a 6 year non-eruptive spreading event that initiated with the June 1999 swarm and cumulatively ruptured and relieved stresses along the whole segment.
- The catalog shows extensive seismic triggering during the 2005 swarms at length scales of up to 50 km and timescales ranging from hours to years. While dynamic triggering may play a role, we argue that static triggering could account for all the observations with the timescale of delays influenced by the timescales of viscoelastic rebound, hydraulic diffusion, and magma withdrawal and replenishment.

Acknowledgments

[58] We thank the officers and crew of the R/V *Thomas G. Thompson* and the R/V *Western Flyer* and the support personnel for the ROVs *ROPOS*, *Tiburon* and *Jason II* for their help with data acquisition. We also thank John Delaney and Deborah Kelley for their leadership of the Keck experiment, and Robert Sohn and Danielle Sumy for thorough reviews of an earlier version of this manuscript. The data acquisition was supported by a grant from the W. M. Keck Foundation with matching support from the University of Washington and the Monterey Bay Aquarium Research Institute. The data analysis was supported by the W. M. Keck Foundation and by NSF under grants OCE-0937006 and OCE-0937285.

References

Barclay, A. H., D. R. Toomey, and S. C. Solomon (2001), Microearthquake characteristics and crustal V_P/V_S structure at the Mid-Atlantic Ridge, 35°N, *J. Geophys. Res.*, *106* (B2), 2017–2034.

Bohnenstiehl, D. R., M. Tolstoy, R. P. Dziak, C. G. Fox, and D. K. Smith (2002), Aftershock sequences in the mid-ocean ridge environment: An analysis using hydroacoustic data, *Tectonophysics*, *354*(1–2), 49–70.

Bohnenstiehl, D. R., R. P. Dziak, M. Tolstoy, C. G. Fox, and M. Fowler (2004), Temporal and spatial history of the 1999–2000 Endeavour Segment seismic series, Juan de Fuca Ridge, *Geochem. Geophys. Geosyst.*, *5*(9), Q09003, doi: 10.1029/2004GC000735.

Brodsky, E. E., and S. G. Prejean (2005), New constraints on mechanisms of remotely triggered seismicity at Long Valley Caldera, *J. Geophys. Res.*, *110*(B4), B04302, doi: 10.1029/2004JB003211.

Brune, J. N. (1970), Tectonic stress and the spectra of seismic shear waves from earthquakes, *J. Geophys. Res.*, *75*(26), 4997–5009.

Buck, W. R., S. M. Carbotte, and C. Mutter (1997), Controls on extrusion at mid-ocean ridges, *Geology*, *25*(10), 935–938.

Carbotte, S. M., M. R. Nedimovic, J. P. Canales, G. M. Kent, A. J. Harding, and M. Marjanovic (2008), Variable crustal structure along the Juan de Fuca Ridge: Influence of on-axis hot spots and absolute plate motions, *Geochem. Geophys. Geosyst.*, *9*(8), Q08001, doi:10.1029/2007GC001922.

Carbotte, S. M., R. S. Detrick, A. Harding, J. P. Canales, J. Babcock, G. Kent, E. Van Ark, M. Nedimovic, and J. Diebold (2006), Rift topography linked to magmatism at the intermediate spreading Juan de Fuca Ridge, *Geology*, *34*(3), doi:10.1130/G21969.1.

Cowen, J. P., E. T. Baker, and R. W. Embley (2004), Detection of and response to mid-ocean ridge magmatic events: Implications for the subsurface biosphere, in *The Subseafloor Biosphere at Mid-Ocean Ridges*, edited by W. S. D. Wilcock, E. F. DeLong, D. S. Kelley, J. A. Baross and S. C. Cary, American Geophysical Union, Washington, DC.

Cowie, P. A., C. H. Scholz, M. Edwards, and A. Malinverno (1993), Fault strain and seismic coupling on mid-ocean ridges, *J. Geophys. Res.*, *98*(B10), 17911–17920.

Crone, T. J., W. S. D. Wilcock, and R. E. McDuff (2010), Flow rate perturbations in a black smoker hydrothermal vent response to a mid-ocean ridge earthquake swarm, *Geochem. Geophys. Geosyst.*, *11*(3), Q03012, doi:10.1029/2009GC002926.

Crone, T. J., M. Tolstoy, and D. F. Stroup (2011), Permeability structure of young ocean crust from poroelastically triggered earthquakes, *Geophys. Res. Lett.*, *38*, L05305, doi:10.1029/2011GL046820.

Cudrak, C. F., and R. M. Clowes (1993), Crustal structure of Endeavour Ridge Segment, Juan de Fuca Ridge, from a detailed seismic refraction survey, *J. Geophys. Res.*, *98*(B4), 6329–6349.

Cummings, W. C., and P. O. Thompson (1971), Underwater sounds from the Blue Whale, Balaenoptera musculus, *J. Acoust. Soc. Am.*, *50*(4), 1193–1198.

Davis, E. E., W. Wang, K. Becker, and R. E. Thompson (2000), Formation-scale hydraulic and mechanical properties of oceanic crust inferred from pore-pressure response to periodic seafloor loading, *J. Geophys. Res.*, *105*(B6), 13423–13435.

Davis, E. E., K. Wang, R. E. Thomson, K. Becker, and J. F. Cassidy (2001), An episode of seafloor spreading and associated plate deformation inferred from crustal fluid pressure transients, *J. Geophys. Res.*, *106*(B10), 21953–21963.

Davis, E. E., K. Becker, R. Dziak, J. Cassidy, K. Wang, and M. Lilley (2004), Hydrological response to a seafloor spreading episode on the Juan de Fuca Ridge, *Nature*, *430*, doi:10.1038/nature02755.

Delaney, J. R., V. Robigou, R. E. McDuff, and M. K. Tivey (1992), Geology of a vigorous hydrothermal system on the Endeavour segment, Juan de Fuca Ridge, *J. Geophys. Res.*, *97*(B13), 19663–19682.

Delaney, J. R., D. S. Kelley, M. D. Lilley, D. A. Butterfield, J. A. Baross, W. S. D. Wilcock, R. W. Embley, and M. Summit (1998), The quantum event of oceanic crustal accretion: Impacts of diking at mid-ocean ridges, *Science*, *281*(5374), 222–230.

deMartin, B. J., R. A. Sohn, J. P. Canales, and S. E. Humphris (2007), Kinematics and geometry of active detachment faulting beneath the Trans-Atlantic Geotraverse (TAG) hydrothermal field on the Mid-Atlantic Ridge, *Geology*, *35*(8), 711–714.

DeMets, C., R. G. Gordon, D. F. Argus, and S. Stein (1994), Effect of recent revisions to the geomagnetic reversal time-scale on estimates of current plate motions, *Geophys. Res. Lett.*, *21*(20), 2191–2194.

Dunn, R. A., D. R. Toomey, and S. C. Solomon (2000), Three-dimensional seismic structure and physical properties of the crust and shallow mantle beneath the East Pacific Rise at 9°30′N, *J. Geophys. Res.*, *105*(B10), 23537–23555.

Dziak, R. P. (2006), Explorer deformation zone: Evidence of a large shear zone and reorganization of the Pacific-Juan de Fuca-North American triple junction, *Geology*, *34*(3), doi:10.1130/g22164.22161.

Dziak, R. P., and C. G. Fox (1999a), Long-term seismicity and ground deformation at Axial Volcano, Juan de Fuca Ridge, *Geophys. Res. Lett.*, *26*(24), 3641–3644.

Dziak, R. P., and C. G. Fox (1999b), The January 1998 earthquake swarm at Axial Volcano, Juan de Fuca Ridge: Hydroacousitc evidence for seafloor volcanic activity, *Geophys. Res. Lett.*, *26*(23), 3429–3432.

Dziak, R. P., C. G. Fox, and A. E. Schreiner (1995), The June–July 1993 seismo-acoustic event at CoAxial segment, Juan de Fuca Ridge: Evidence for a lateral dike injection, *Geophys. Res. Lett.*, *22*(2), 135–138.

Dziak, R. P., S. R. Hammond, and C. G. Fox (2011), A 20-year hydroacoustic time series of seismic and volcanic events in the Northeast Pacific Ocean, *Oceanography*, *24*(3), 280–293.

Dziak, R. P., D. R. Bohnenstiehl, J. P. Cowen, E. T. Baker, K. H. Rubin, J. H. Haxel, and M. J. Fowler (2007), Rapid dike emplacement leads to eruptions and hydrothermal plume release during seafloor spreading events, *Geology*, *35*(7), doi:10.1130/G23476a.23471.

Dziak, R. P., D. K. Smith, D. R. Bohnenstiehl, C. G. Fox, D. Desbruyeres, H. Matsumoto, M. Tolstoy, and D. J. Fornari (2004), Evidence of a recent magma dike intrusion at the slow spreading Lucky Strike segment, Mid-Atlantic Ridge, *J. Geophys. Res.*, *109*(B12), B12102, doi:10.1029/2004JB003141.

Ebinger, C., A. Ayele, D. Keir, J. Rowland, G. Yirgu, T. Wright, M. Belachew, and I. Hamling (2010), Length and timescales of rift faulting and magma intrusion: The Afar Rifting Cycle from 2005 to present, *Ann. Rev. Earth Planet. Sci.*, *38*, doi:10.1146/annurev-earth-040809-152333.

Fisher, A. T. (1998), Permeability within basaltic oceanic crust, *Rev. Geophys.*, *36*(2), 143–182.

Fox, C. G., and D. P. Dziak (1998), Hydroacoustic detection of volcanic activity on the Gorda Ridge, February–March 1996, *Deep-Sea Res. Part II*, *45*(12), 2513–2530.

Freed, A. M. (2005), Earthquake triggering by static, dynamic, and postseismic stress transfer, *Ann. Rev. Earth Planet. Sci.*, *33*, doi:10.1146/annurev.earth.1133.092203.122505.

Freed, A. M., and J. Lin (1998), Time-dependent changes in failure stress following thrust earthquakes, *J. Geophys. Res.*, *103*(B10), 24393–24409.

Freed, A. M., and J. Lin (2001), Delayed triggering of the 1999 Hector Mine earthquake by viscoelastic stress transfer, *Nature*, *411*, 180–183.

Glickson, D. A., D. S. Kelley, and J. R. Delaney (2007), Geology and hydrothermal evolution of the Mothra hydrothermal field, Endeavour Segment, Juan de Fuca Ridge, *Geochem. Geophys. Geosyst.*, *8*(6), Q06010, doi:10.1029/2007GC001588.

Gomberg, J., P. A. Reasenberg, P. Bodin, and R. A. Harris (2001), Earthquake triggering by seismic waves following the Landers and Hector Mine earthquakes, *Nature*, *411*(6836), 462–466.

Grandin, R., A. Socquet, C. Doubre, E. Jacques, and G. C. P. King (2012), Elastic thickness control of lateral dyke

intrusion at mid-ocean ridges, *Earth Planet. Sci. Lett.*, *319–320*(2012), doi:10.1016/j.epsl.2011.1012.1011.

Hanks, T. C., and M. Wyss (1972), The use of body-wave spectra in the determination of seismic-source parameters, *Bull. Seismol. Soc. Am.*, *62*(2), 561–589.

Hanks, T. C., and H. Kanamori (1979), Moment magnitude scale, *J. Geophys. Res.*, *84*(B5), 2348–2350.

Hardebeck, J. L., J. J. Nazareth, and E. Hauksson (1998), The static stress change triggering model: Constraints from two southern California aftershock sequences, *J. Geophys. Res.*, *103*(B10), 24427–24437.

Harris, R. A., and R. W. Simpson (1992), Changes in static stress on Southern California faults after the 1992 Landers earthquake, *Nature*, *360*(6401), 251–254.

Hill, D. P. et al. (1993), Seismicity remotely triggered by the magnitude 7.3 Landers, California, earthquake, *Science*, *260*(5114), 1617–1623.

Hirth, G., and D. L. Kohlstedt (1996), Water in the oceanic upper mantle: Implications for rheology, melt extraction and the evolution of the lithosphere, *Earth Planet. Sci. Lett.*, *144*, 93–108.

Hirth, G., J. Escartin, and J. Lin (1998), The rheology of the lower oceanic crust: Implications for lithospheric deformation at mid-ocean ridges, *Geophys. Monogr.*, *106*, 291–303.

Hooft, E. E. E., et al. (2010), A seismic swarm and regional hydrothermal and hydrologic perturbations: The northern Endeavour segment, February 2005, *Geochem. Geophys. Geosyst.*, *11*(12), Q12015, doi:10.1029/2010GC003264.

Huang, P. Y., S. C. Solomon, E. A. Bergman, and J. L. Nabelek (1986), Focal depths and mechanisms of Mid-Atlantic Ridge earthquakes from body wave-form inversion, *J. Geophys. Res.*, *91*(B1), 579–598.

Hyndman, R. D., R. P. Riddihough, and R. Herzer (1979), The Nootka fault zone—A new plate boundary off western Canada, *Geophys. J. Roy. Astron. Soc.*, *58*, 667–683.

Johnson, H. P., M. Hutnak, R. P. Dziak, C. G. Fox, I. Urcuyo, J. P. Cowen, J. Nabalek, and C. Fisher (2000), Earthquake-induced changes in a hydrothermal system on the Juan de Fuca Ridge mid-ocean ridge, *Nature*, *407*, 174–177.

Karson, J. A. et al. (1987), Along-axis variations in seafloor spreading in the MARK area, *Nature*, *328*, 681–685.

Karsten, J. L., and J. R. Delaney (1989), Hot spot-ridge crest convergence in the Northeast Pacific, *J. Geophys. Res.*, *94*(B1), 700–712.

Karsten, J. L., S. R. Hammond, E. E. Davis, and R. G. Currie (1986), Detailed geomorphology and neotectonics of the Endeavour Segment, Juan de Fuca Ridge—New results from Seabeam swath mapping, *Geol. Soc. Am. Bull.*, *97*(2), 213–221.

Karsten, J. L., J. R. Delaney, J. M. Rhodes, and R. A. Liias (1990), Spatial and temporal evolution of magmatic systems beneath the Endeavour segment, Juan de Fuca Ridge: Tectonic and petrologic constraints, *J. Geophys. Res.*, *95*(B12), 19,235–219,256.

Kelley, D. S., J. R. Delaney, and D. R. Yoerger (2001), Geology and venting characteristics of the Mothra hydrothermal field, Endeavour Segment, Juan de Fuca Ridge, *Geology*, *29*(10), 959–962.

Kelley, D. S., J. A. Baross, and J. R. Delaney (2002), Volcanoes, fluids, and life at mid-ocean ridge spreading centers, *Ann. Rev. Earth Planet. Sci.*, *30*, 385–491.

Kent, G. M. et al. (2000), Evidence from three-dimensional seismic reflectivity images for enhanced melt supply beneath mid-ocean-ridge discontinuities, *Nature*, *406*(6796), 614–618.

Kilb, D., J. Gomberg, and P. Bodin (2000), Triggering of earthquake aftershocks by dynamic stresses, *Nature*, *408*(6812), 570–574.

King, G. C. P., R. S. Stein, and J. Lin (1994), Static stress changes and the triggering of earthquakes, *Bull. Seismol. Soc. Am.*, *84*(3), 935–953.

Klein, F. W. (2002), User's guide to HYPOINVERSE-2000, a Fortran program to solve for earthquake locations and magnitudes, *U. S. Geol. Surv. Open File Rep. Rep. 02-171*, 123.

Kreemer, C., R. Govers, K. P. Furlong, and W. E. Holt (1998), Plate boundary deformation between the Pacific and North America in the Explorer region, *Tectonophysics*, *293*, 225–238.

Lilley, M. D., D. A. Butterfield, J. E. Lupton, and E. J. Olson (2003), Magmatic events can produce rapid changes in hydrothermal vent chemistry, *Nature*, *422*, 878–881.

Lowell, R. P., and L. N. Germanovich (1994), On the temporal evolution of high-temperature hydrothermal systems at ocean ridge crests, *J. Geophys. Res.*, *99*(B1), 565–575.

Macdonald, K. C. (1998), Linkages between faulting, volcanism, hydrothermal activity and segmentation on fast spreading centers, in *Faulting and Magmatism at Mid-ocean Ridges*, edited by W. R. Buck, P. T. Delaney, J. A. Karson and Y. Lagabrielle, American Geophysical Union, Washington, D.C.

Macdonald, K. C. (2001), *Mid-Ocean Ridge Tectonics, Volcanism and Geomorphology*, Academic Press, San Diego, Calif.

McClain, J. S., M. L. Begnaud, M. A. Wright, J. Fondrk, and G. K. Von Damm (1993), Seismicity and tremor in a submarine hydrothermal field: The northern Juan de Fuca Ridge, *Geophys. Res. Lett.*, *20*(17), 1883–1886.

Nostro, C., M. Cocco, and M. E. Belardinelli (1997), Static stress changes in extensional regimes: An application to southern Apennines (Italy), *Bull. Seismol. Soc. Am.*, *87*(1), 234–248.

Nostro, C., A. Piersanti, and M. Cocco (2001), Normal fault interaction caused by coseismic and postseismic stress changes, *J. Geophys. Res.*, *106*(B9), 19391–19410.

Parmentier, E. M., and J. Phipps Morgan (1990), Spreading rate dependence of three-dimensional structure in oceanic spreading centers, *Nature*, *348*, 325–328.

Phipps Morgan, J., and Y. J. Chen (1993), Dependence of ridge-axis morphology on magma supply and spreading rate, *Nature*, *364*, 706–708.

Prejean, S. G., D. P. Hill, E. E. Brodsky, S. E. Hough, M. J. S. Johnston, S. D. Malone, D. H. Oppenheimer, A. M. Pitt, and K. B. Richards-Dinger (2004), Remotely triggered seismicity from the United States west coast following the M_w 7.9 Denali Fault Earthquake, *Bull. Seismol. Soc. Am.*, *94*(6), 348–359.

Qin, R., and W. R. Buck (2008), Why meter-wide dikes at oceanic spreading centers?, *Earth Planet. Sci. Lett.*, *265*(3–4), doi:10.1016/j.epsl.2007.1010.1044.

Robigou, V., J. R. Delaney, and D. S. Stakes (1993), Large massive sulfide deposits in a newly discovered active hydrothermal system, the High-Rise field, Endeavour segment, Juan de Fuca Ridge, *Geophys. Res. Lett.*, *20*(17), 1887–1890.

Romanowicz, B., D. Stakes, D. Dolenc, D. Neuhauser, P. McGill, R. Uhrhammer, and T. Ramirez (2006), The Monterey Bay broadband ocean bottom seismic observatory, *Ann. Geophys.*, *49*(2–3), 607–623.

Rubin, K. H., S. A. Soule, W. W. Chadwick, D. J. Fornari, D. S. Clague, R. W. Embley, E. T. Baker, M. R. Perfit, D. W. Caress, and R. P. Dziak (2012), Volcanic Eruptions in the Deep Sea, *Oceanogr.*, *25*, 142–157, doi:http://dx.doi.org/10.5670/oceanog.2012.12.

Rubin, K. H., J. D. Macdougall, and M. R. Perfit (1994), ^{210}Po–^{210}Pb dating of recent volcanic-eruptions on the sea-floor, *Nature*, *368*(6474), 841–844.

Seewald, J., A. Cruse, and P. Saccocia (2003), Aqueous volatiles in hydrothermal fluids from the Main Endeavour Field, northern Juan de Fuca Ridge: temporal variability followig earthquake activity, *Earth Planet. Sci. Lett.*, *216*(4), doi:10.1016/S0012-821X(03)00543-0.

Seyfried, W. E., Jr., J. S. Seewald, M. E. Berndt, K. Ding, and D. I. Foustoukos (2003), Chemistry of hydrothermal vent fluids from the Main Endeavour Field, northern Juan de Fuca Ridge: Geochemical controls in the aftermath of the June 1999 seismic events, *J. Geophys. Res.*, *108*(B9), 2429, doi:10.1029/2002JB001957.

Shi, Y., and B. A. Bolt (1982), The standard error of the magnitude-frequency b-value, *Bull. Seismol. Soc. Am.*, *72*(5), 1677–1687.

Sigmundsson, F. (2006), *Iceland Geodynamics: Crustal Deformation and Divergent Plate Tectonics*, Praxis Publishing: Chichester, United Kingdom; Springer-Verlag: Berlin, United Kingdom.

Sinton, J. M., and R. S. Detrick (1992), Mid-ocean ridge magma chambers, *J. Geophys. Res.*, *97*(B1), 197–216.

Smith, D. K., and J. R. Cann (1992), The role of seamount volcanism in crustal construction at the Mid-Atlantic Ridge (24°–30°N), *J. Geophys. Res.*, *97*(B2), 1645–1658.

Smith, D. K., and J. R. Cann (1993), Building the crust at the Mid-Atlantic Ridge, *Nature*, *365*, 707–715.

Sohn, R. A., J. A. Hildebrand, and S. C. Webb (1998a), Postrifting seismicity and a model for the 1993 diking event on the CoAxial segment, Juan de Fuca Ridge, *J. Geophys. Res.*, *103*(B5), 9867–9877.

Sohn, R. A., W. C. Crawford, and S. C. Webb (1999), Local seismicity following the 1998 eruption of Axial Volcano, *Geophys. Res. Lett.*, *26*(23), 3433–3436.

Sohn, R. A., A. H. Barclay, and S. C. Webb (2004), Microearthquake patterns following the 1998 eruption of Axial Volcano, Juan de Fuca Ridge: Mechanical relaxation and thermal strain, *J. Geophys. Res.*, *109*(B1), B01101, doi:10.1029/2003JB002499.

Sohn, R. A., D. J. Fornari, K. L. Von Damm, J. A. Hildebrand, and S. C. Webb (1998b), Seismic and hydrothermal evidence for a cracking event on the East Pacific rise crest at 9º50′N, *Nature*, *396*, 159–161.

Spera, F. J. (2000), *Physical Properties of Magmas*, Academic Press, San Diego, CA, pp. 171–190.

Stakes, D., J. McClain, T. VanZandt, P. McGill, and M. Begnaud (1998), Corehole seismometer development for low-noise seismic data in a long-term seafloor observatory, *Geophys. Res. Lett.*, *25*(14), 2745–2748.

Stakes, D., B. Romanowicz, M. L. Begnaud, K. C. McNally, J. P. Montagner, E. Stutzmann, and M. Pasyanos (2002), The MBARI margin seismology experiment: A propotype seafloor observatory, in *Science-Technology Synergy for Research in the Marine Environment: Challanges for the XXI Century*, edited by L. Bernazoli, P. Favali and G. Smriglio, pp. 93–110, Elsevier, Amsterdam, The Netherlands.

Stein, R. S., A. A. Barka, and J. H. Dieterich (1997), Progressive failure on the North Anatolian fault since 1939 by earthquake stress triggering, *Geophys. J. Int.*, *128*(3), 594–604.

Stroup, D. F., M. Tolstoy, T. J. Crone, A. Malinverno, D. R. Bohnenstiehl, and F. Waldhauser (2009), Systematic along-axis tidal triggering of microearthquakes observed at 9 degrees 50′N East Pacific Rise, *Geophys. Res. Lett.*, *36*, L18302, doi:10.1029/2009GL039493.

Takanami, T., and G. Kitagawa (1988), A new efficient procedure for the estimation of onset times of seismic waves, *J. Phys. Earth*, *36*, 267–290.

Tolstoy, M. (2008a), Seismic identification of along-axis hydrothermal flow on the East Pacific Rise, *Nature [London]*, *451*(7175), 181–184.

Tolstoy, M. (2008b), Seismological constraints on magmatic and hydrothermal proceses at mid-ocean ridges, in *Modeling Hydrothermal Processes at Oceanic Spreading Centers*, edited by R. P. Lowell, J. S. Seewald, A. Metaxas, and M. R. Perfit, American Geophysical Union, Washington, D.C.

Tolstoy, M., F. Waldhauser, D. R. Bohnenstiehl, R. T. Weekly, and W. Y. Kim (2008), Seismic identification of along-axis hydrothermal flow on the East Pacific Rise, *Nature*, *451*(7175), doi:10.1038/Nature06424.

Tolstoy, M. et al. (2006), A sea-floor spreading event captured by seismometers, *Science*, *314*(5807), doi:10.1126/Science.1133950.

Toomey, D. R., S. C. Solomon, and G. M. Purdy (1988), Microearthquakes beneath median valley of the Mid-Atlantic Ridge near 23°N: Tomography and tectonics, *J. Geophys. Res.*, *93*(B8), 9093–9112.

Toomey, D. R., S. C. Solomon, G. M. Purdy, and M. H. Murray (1985), Microearthquakes beneath the median valley of the Mid-Atlantic Ridge near 23°N: Hypocenters and focal mechanisms, *J. Geophys. Res.*, *90*(B7), 5443–5458.

Toomey, D. R., D. Jousselin, R. A. Dunn, W. S. D. Wilcock, and R. S. Detrick (2007), Skew of mantle upwelling beneath the East Pacific Rise governs segmentation, *Nature*, *446*(7134), 409–414.

Tréhu, A. M., and S. C. Solomon (1983), Earthquakes in the Orozco transform zone: Seismicity, source mechanisms, and tectonics, *J. Geophys. Res.*, *88*, 8203–8225.

Turcotte, D. L., and G. Schubert (2002), *Geodynamics: Applications of Continuum Mechanics to Geological Problems*, 2nd ed., Cambridge University Press, New York, NY, pp. 456.

Van Ark, E. M., R. S. Detrick, J. P. Canales, S. M. Carbotte, A. J. Harding, G. M. Kent, M. R. Nedimovic, W. S. D. Wilcock, J. B. Diebold, and J. M. Babcock (2007), Seismic structure of the Endeavour Segment, Juan de Fuca Ridge: Correlations with seismicity and hydrothermal activity, *J. Geophys. Res.*, *112*(B2), B02401, doi:10.1029/2005JB004210.

Watkins, W. A., P. Tyack, and K. E. Moore (1987), The 20-Hz signals of finback whales (Balaenoptera physalus), *J. Acoust. Soc. Am.*, *82*(6), 1901–1912.

Weekly, R. T., W. S. D. Wilcock, D. R. Toomey, E. E. E. Hooft, and A. Wells (2011), Upper- to mid-crustal velocity structure of the endeavour segment: Implications for crustal construction, *EOS Trans. AGU*, Fall Meet. Suppl., Abstract V11E-2552.

Wiemer, S., and M. Wyss (2002), Mapping spatial variability of the frequency-magnitude distribution of earthquakes, *Adv. Geophys.*, *45*, 259–302.

Wilcock, W. S. D., and A. McNabb (1996), Estimates of crustal permeability on the Endeavour segment of the Juan de Fuca mid-ocean ridge, *Earth Planet. Sci. Lett.*, *138*(1–4), 83–91.

Wilcock, W. S. D., and J. R. Delaney (1996), Mid-ocean ridge sulfide deposits: Evidence for heat extraction from magma chambers or cracking fronts?, *Earth Planet. Sci. Lett.*, *145*, 49–64.

Wilcock, W. S. D., S. D. Archer, and G. M. Purdy (2002), Microearthquakes on the Endeavour segment of the Juan de Fuca Ridge, *J. Geophys. Res.*, *107*(B12), 2336, doi:10.1029/2001JB000505.

Wilcock, W. S. D., E. E. E. Hooft, D. R. Toomey, P. R. McGill, A. H. Barclay, D. S. Stakes, and T. M. Ramirez (2009), The role of magma injection in localizing black smoker activity, *Nature Geosci.*, doi:10.1038/NGEO1550.

Wilcock, W. S. D., P. R. McGill, E. E. E. Hooft, D. R. Toomey, H. M. Patel, D. S. Stakes, A. H. Barclay, T. M. Ramirez, and R. T. Weekly (2007), The deployment of a long-term seismic network on the Juan de Fuce Ridge, paper presented at Oceans 2007, Vancouver, Canada, September 29–October 1.

Wolfe, C. J., G. M. Purdy, D. R. Toomey, and S. C. Solomon (1995), Microearthquake characteristics and crustal velocity structure at 29°N on the Mid-Atlantic Ridge: The architecture of a slow spreading segment, *J. Geophys. Res.*, *100*(B12), 24449–24472.